Supplementary Information for

Harnessing ion-dipole interactions: A simple and effective approach to high-performance lithium receptors

Chengkai Xu, Quy Tran, Lukasz Wojtas, Wenqi Liu*

Department of Chemistry, 4202 E. Fowler Ave, University of South Florida, Tampa, FL, 33620, USA

*wenqi@usf.edu

Table of Contents

1. General Method.

All Commercially available solvents and chemicals were purchased from Sigma-Aldrich and Fisher Scientific and used without further purification unless otherwise stated. 2,2-dibenzylpropane-1,3-diol,[S1] dibenzo-14-crown-4, [S2] and I1 [S3] were synthesized according to the reported literature. Water was deionized and micro-filtered through a Milli-Q water filtration system. Reactions were monitored by analytical thin-layer chromatography (TLC) on silica gel 60-F_{254} plates, visualized by ultraviolet (254 nm). Nuclear magnetic resonance (NMR) spectra were recorded on Varian Unity Inova 600 MHz spectrometer or Varian Unity Inova 400 MHz system. The chemical shift was presented in ppm and referenced by residual non-deuterated solvent peaks ($CDCl_3$: δ = 7.26 ppm, CD_3CN: δ = 1.94 ppm). High-resolution mass spectrometry (HRMS) was performed by Waters Synapt G2 mass spectrometer using an ESI source. Flash Column chromatography was performed using a Biotage Selekt system with silica gel (silicaFlash P60 from SILICYCLE) as the stationary phase. Isothermal titration was performed on the MicroCal iTC_{200} system, and samples were filtered through a 0.45 μm PTFE filter before use. ITC Data were analyzed on MicroCal iTC_{200} software. Detailed experimental procedures are provided below in the appropriate sections of this supplementary information.

2. Synthesis and Compound Characterization

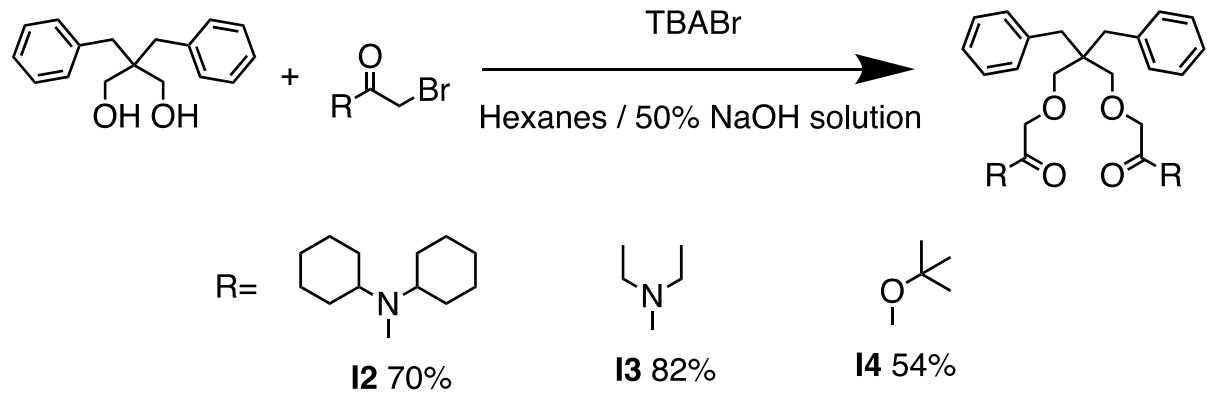

Scheme S1. Synthesis of I2-I4

General Procedure for the synthesis of I2–I4: 2,2-dibenzylpropane-1,3-diol (1.0 mmol, 1.0eq) was added to a mixture of hexane (5 mL) and 50% NaOH solution (5 mL, w/v). The 2-bromoacetamides or 2-bromoacetate (2.2 mmol, 2.2eq.) were added in a small portion. The resulting suspension was stirred vigorously for 12 h at room temperature. The reaction mixture was diluted with H_2O (50 mL) and extracted with EtOAc (3 × 30 mL). The organic phase was combined and washed with brine (2×30 mL). The solvent was removed under vacuum, and the residue was purified by flash column chromatography (hexanes / EtOAc).

I2: The title compound I2 was prepared and purified by flash column chromatography (hexanes / EtOAc = 9: 1). I2 was obtained as a white solid. ^{1}H NMR (600 MHz, $CDCl_3$) δ 7.27 – 7.15 (m, 10H), 4.01 (s, 4H), 3.59 (s, 2H), 3.17 (s, 4H), 2.94 (s, 2H), 2.82 (s, 4H), 2.48 (s, 4H), 1.86 – 1.23 (m, 36 H); ^{13}C NMR (151 MHz, $CDCl_3$) δ 167.9, 151.5, 130.8, 128.0, 72.7, 38.8, 31.5, 29.9, 26.6, 26.0, 25.4, 25.3. HRMS-ESI: calcd for $C_{45}H_{66}N_2O_4$: 699.5095 $[M+H]^+$; found: 699.5082.

I3: The title compound I3 was prepared and purified by flash column chromatography (hexanes / EtOAc = 9: 1). I3 was obtained as a white solid. ^{1}H NMR (600 MHz, $CDCl_3$) δ 7.44 – 7.02 (m, 10H), 4.09 (s, 4H), 3.43 – 3.35 (m, 7H), 3.17 (s, 4H), 2.84 (s, 4H), 1.21 (t, J = 7.1 Hz, 6H), 1.14 (t, J = 7.1 Hz, 6H). ^{13}C NMR (151 MHz, $CDCl_3$) δ 168.1, 137.9, 130.8, 128.0, 126.1, 72.6, 70.8, 43.8, 41.2, 40.0, 38.8, 14.5, 12.9. HRMS-ESI: calcd for $C_{29}H_{40}O_{6:}$ 507.2717 $[M+Na]^+$; found: 507.2700

I4: The title compound I4 was prepared and purified by flash column chromatography (hexanes / EtOAc = 9 : 1). I4 was obtained as a colorless oil. ^{1}H NMR (600 MHz, $CDCl_3$) δ 7.27 (d, J = 4.4 Hz, 8H), 7.20 (h, J = 4.3 Hz, 2H), 3.94 (s, 4H), 3.13 (s, 4H), 2.85 (s, 4H), 1.47 (s, 18H).

^{1}H NMR (400 MHz, $CDCl_3$) δ 7.30 – 7.25 (m, 4H), 7.22 – 7.17 (m, 4H), 4.09 (s, 4H), 3.39 (m, 8H), 3.17 (s, 4H), 2.84 (s, 4H), 1.21 (t, J = 7.1 Hz, 6H), 1.14 (t, J = 7.1 Hz, 6H); ^{13}C NMR (151 MHz, $CDCl_3$) δ 169.5, 138.1, 130.9, 127.9, 126.0, 81.4, 77.2, 77.0, 76.8, 72.4, 69.5, 43.8, 38.6, 28.1; HRMS-ESI: calcd for $C_{27}H_{42}O_4N_2$ 483.3217 $[M+H]^+$; found: 483.3196

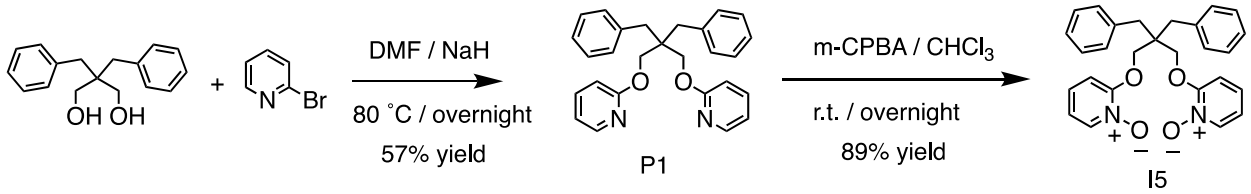

Scheme S2. Synthesis of I5

P1: To a solution of 2,2-dibenzylpropane-1,3-diol (1.95 mmol, 1.0eq., 500mg) in dry DMF(15mL) was added NaH (3.0eq., 204mg, 60% in mineral oil) in portions. The mixture was stirred for one h at room temperature. 2-Bromopyridine (4.88mmol, 2.5eq., 770mg) was then added dropwise. When the addition was done, the temperature was raised to 80 ˚C and stirred overnight. The reaction was quenched with water, poured into ice water (150mL), and extracted by ethyl acetate (3×30mL). The combined organic phase was washed with water (3×30mL) and brine (2×30mL). The solvent was removed under vacuum, and the residue was purified by flash column chromatography (hexanes / EtOAc) to afford precursor P1 (57%, 460mg) as a white solid. ^{1}H NMR (400 MHz, $CDCl_3$) δ 8.13 (dd, *J* = 5.1, 2.0 Hz, 2H), 7.66 – 7.58 (m, 2H), 7.15 (m, 10H), 6.92 – 6.82 (m, 4H), 4.01 (s, 4H), 3.05 (s, 4H). ^{13}C NMR (151 MHz, $CDCl_3$) δ 163.7, 147.2, 138.6, 137.5, 130.7, 128.1, 126.2, 116.8, 110.9, 66.0, 42.9, 39.2. HRMS-ESI: calcd for $C_{27}H_{26}N_2O_2$ $[M+H]^+$: 410.1994 found: 410.1999.

I5: To a solution of precursor P1 (200mg, 0.49mmol, 1.0eq.) in $CHCl_3$ (5mL), m-CPBA (1.46mmol, 3.0eq., 252mg) was added, and the reaction stirred overnight. The solvent was removed under reduced pressure, and the crude product was purified by column chromatography (0~15% methanol in DCM) to afford I5 (192mg, 89%) as a white solid. ^{1}H NMR (400 MHz, $CDCl_3$) δ 8.27 (dd, *J* = 6.4, 1.6 Hz, 2H), 7.36 – 7.30 (m, 4H), 7.30 – 7.17 (m, 10H), 6.97 – 6.85 (m, 4H), 4.09 (s, 4H), 3.19 (s, 4H). ^{13}C NMR (101 MHz, $CDCl_3$) δ 158.1, 140.3, 136.4, 130.9, 128.4, 127.6, 126.7, 118.0, 110.4, 71.4, 43.6, 37.5. HRMS-ESI: calcd for $C_{27}H_{26}N_2O_4$ $[M+H]^+$: 410.1895 found: 442.1893.

3. Mass Spectrometry

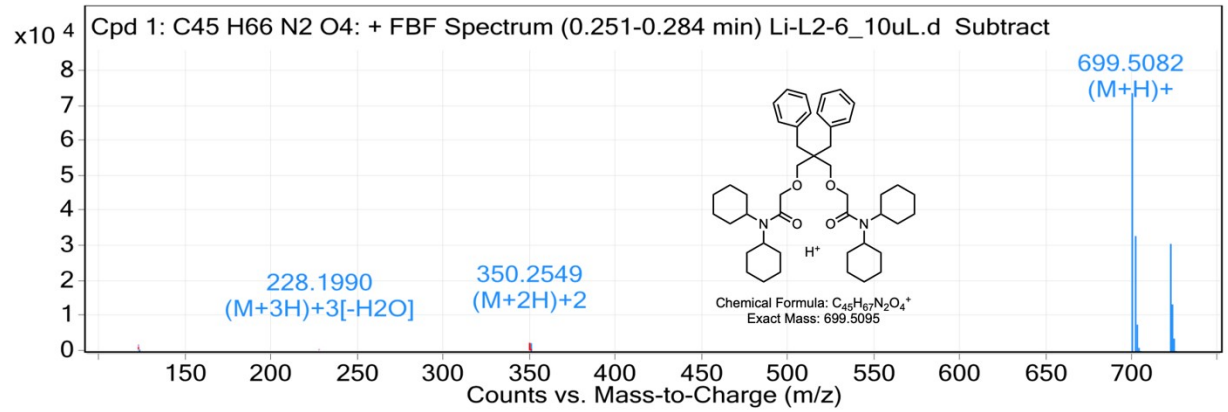

Figure S1. HRMS-ESI of I2.

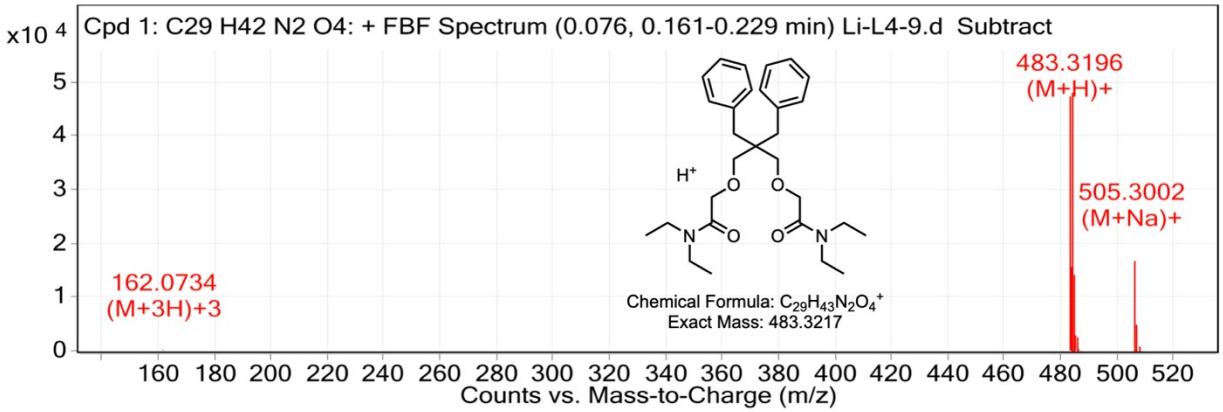

Figure S2. HRMS-ESI of I3.

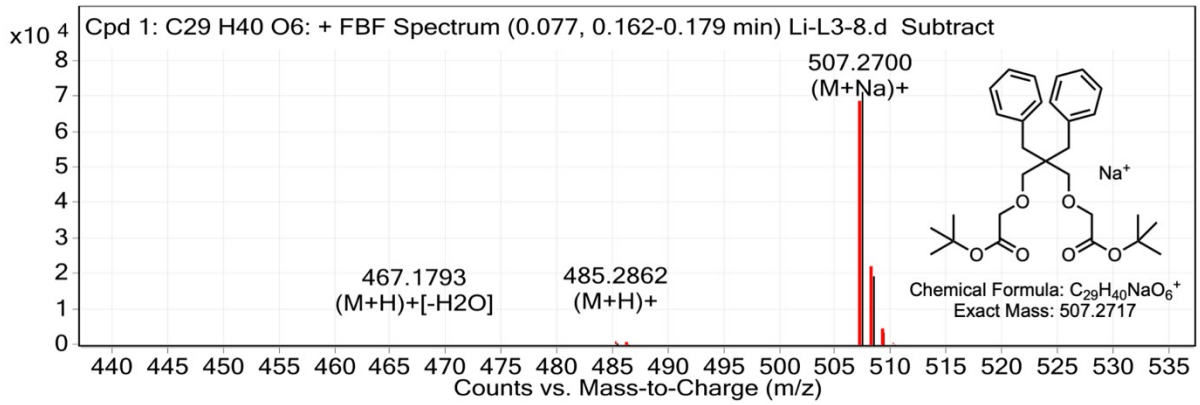

Figure S3. HRMS-ESI of I4.

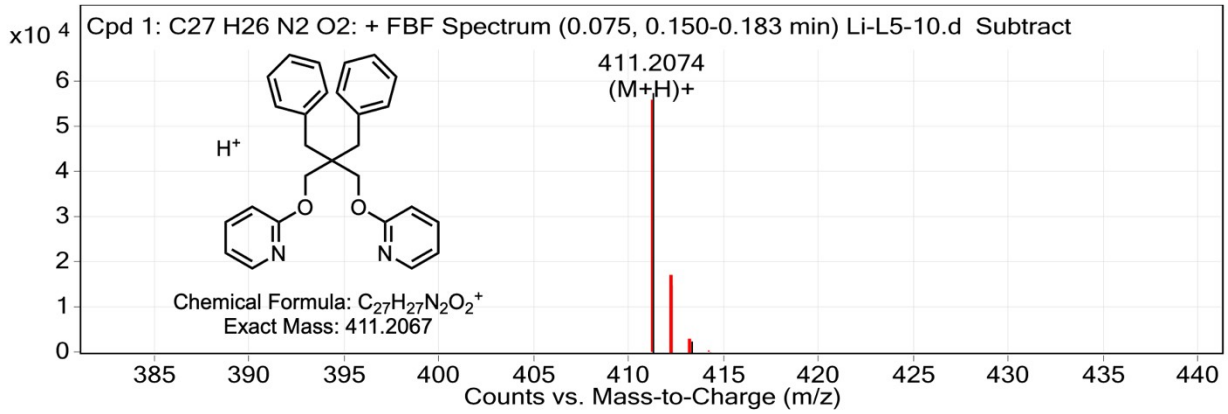

Figure S4. HRMS-ESI of precursor P1.

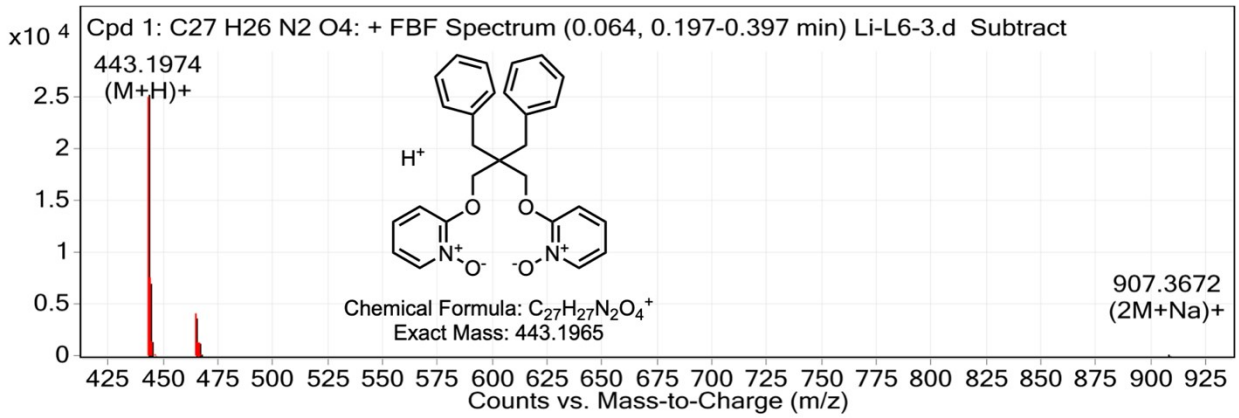

Figure S5. HRMS-ESI of I5.

4. NMR Spectroscopy

Compound Characterization

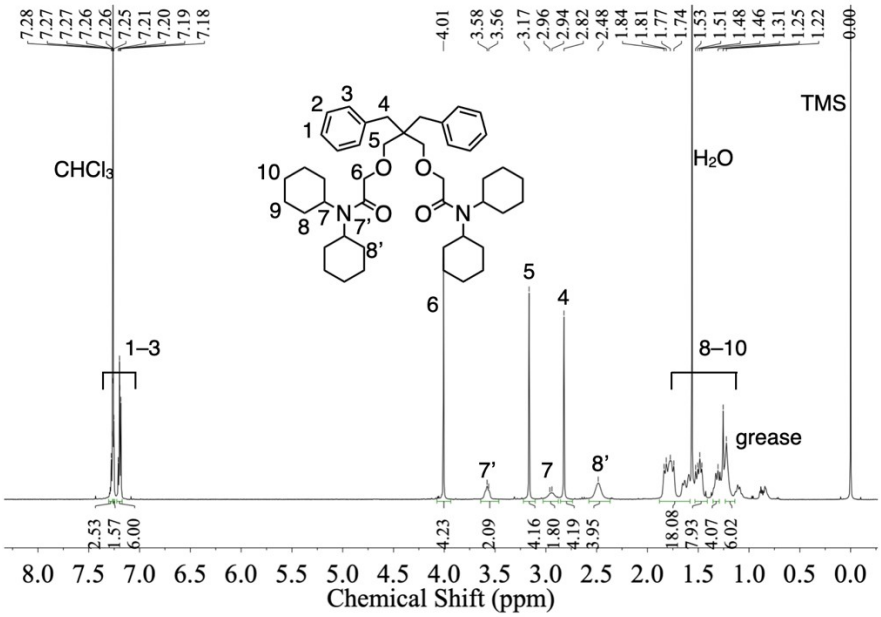

Figure S6. ^{1}H NMR (600MHz, $CDCl_3$) spectrum of I2.

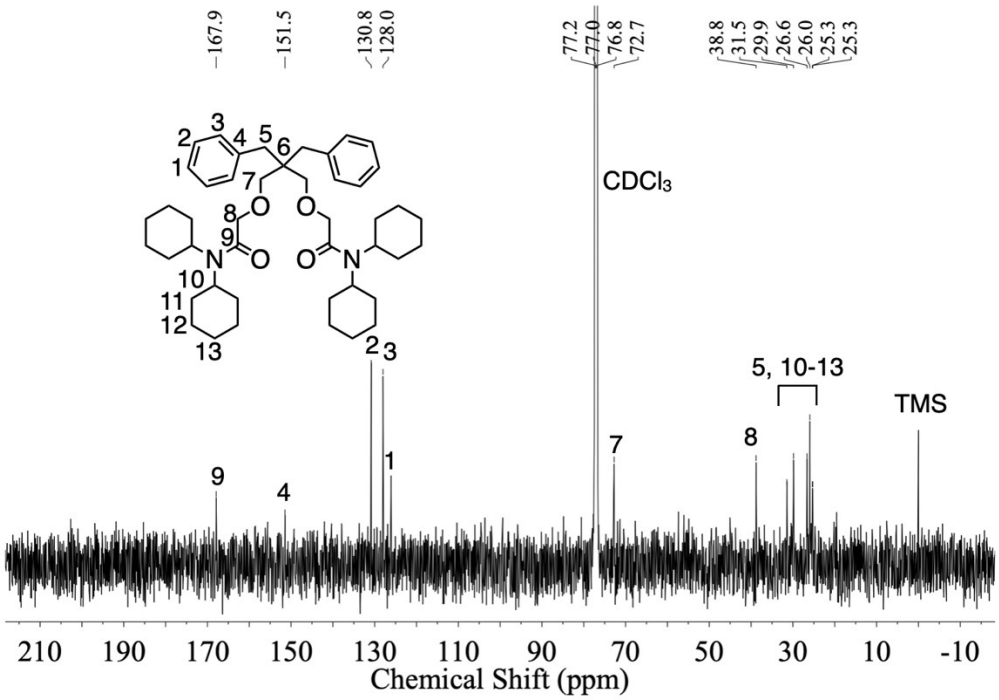

Figure S7. ^{13}C NMR (151 MHz, $CDCl_3$) spectrum of I2.

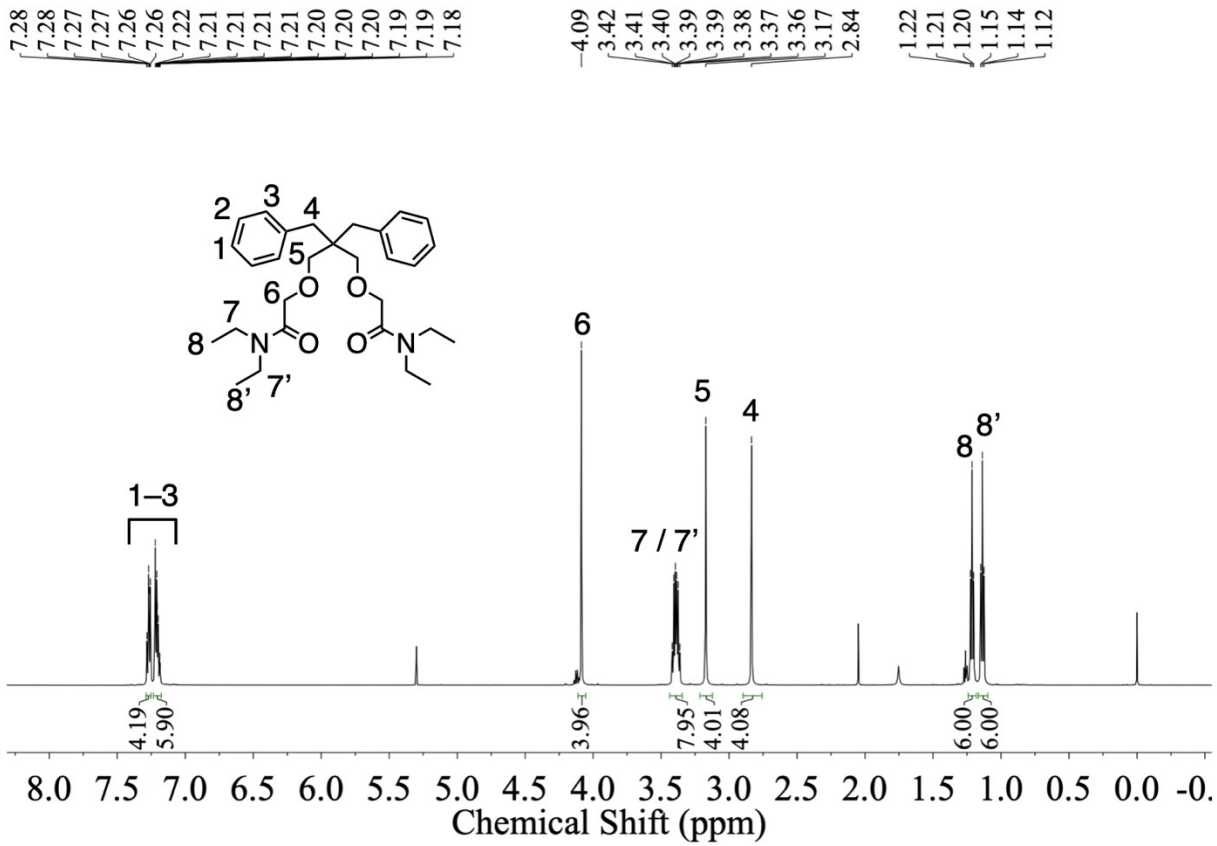

Figure S8. ^{1}H NMR (600MHz, $CDCl_3$) spectrum of I3.

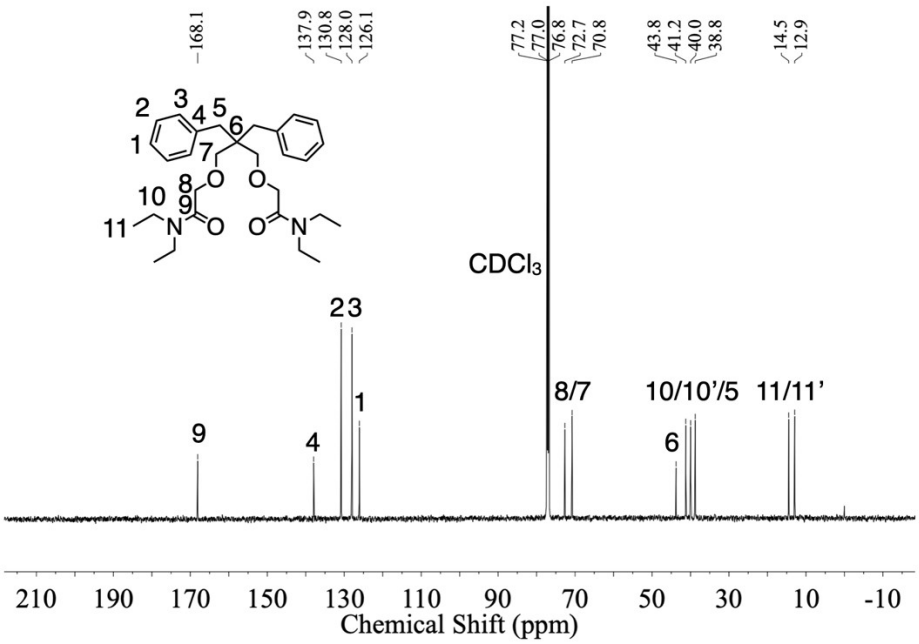

Figure S9. ^{13}C NMR (151 MHz, $CDCl_3$) spectrum of I3.

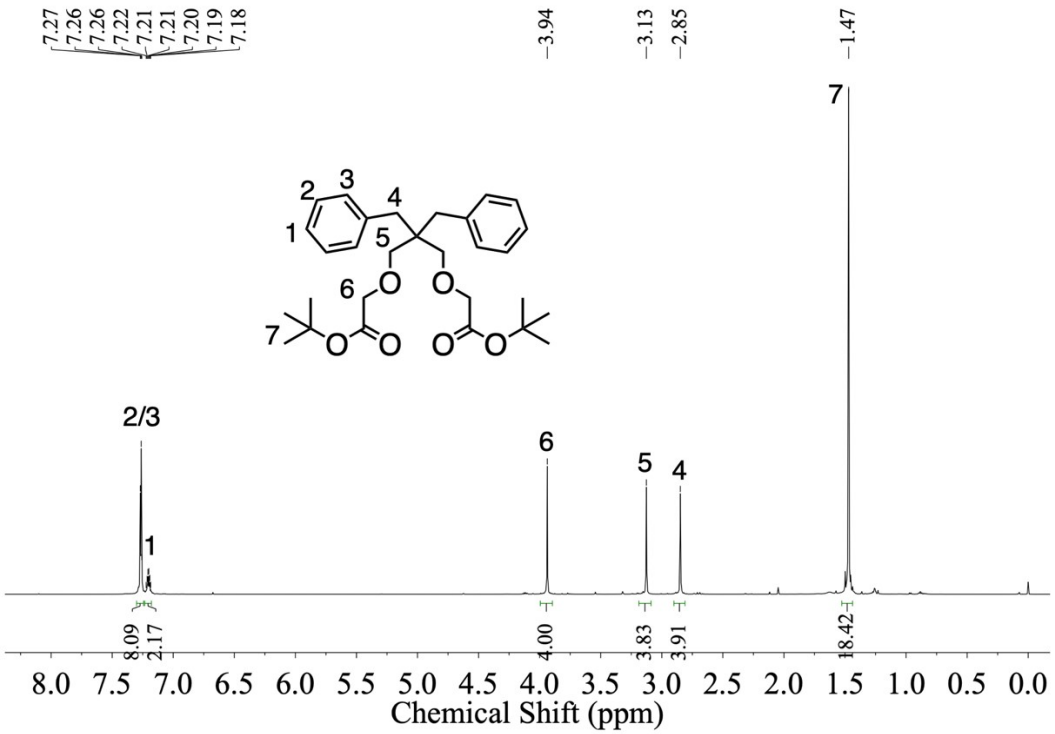

Figure S10. ^{1}H NMR (600MHz, $CDCl_3$) spectrum of I4.

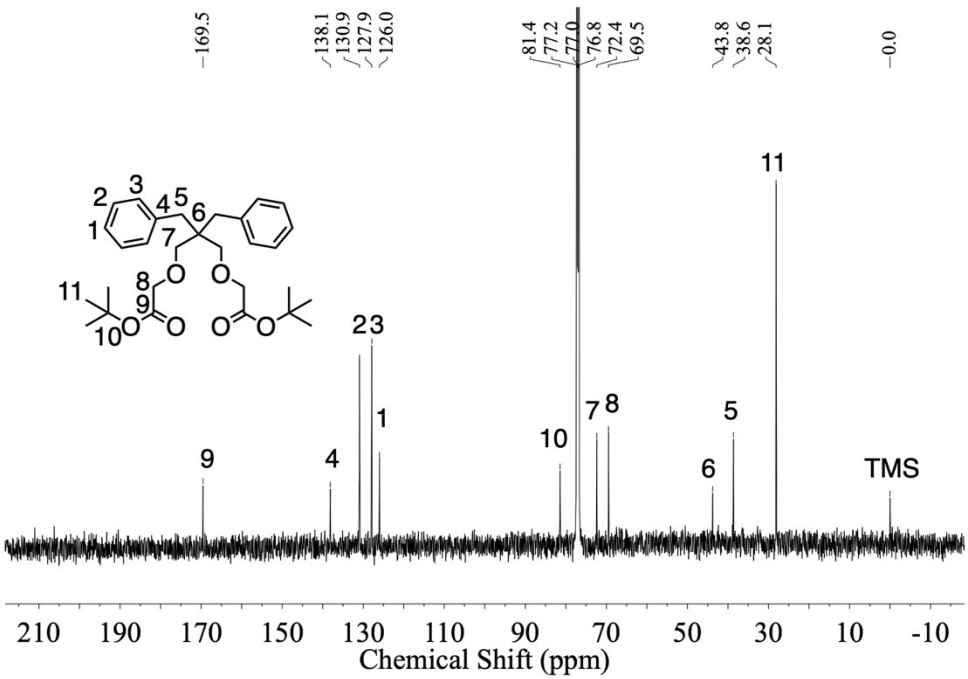

Figure S11. ^{13}C NMR (151 MHz, $CDCl_3$) spectrum of I4.

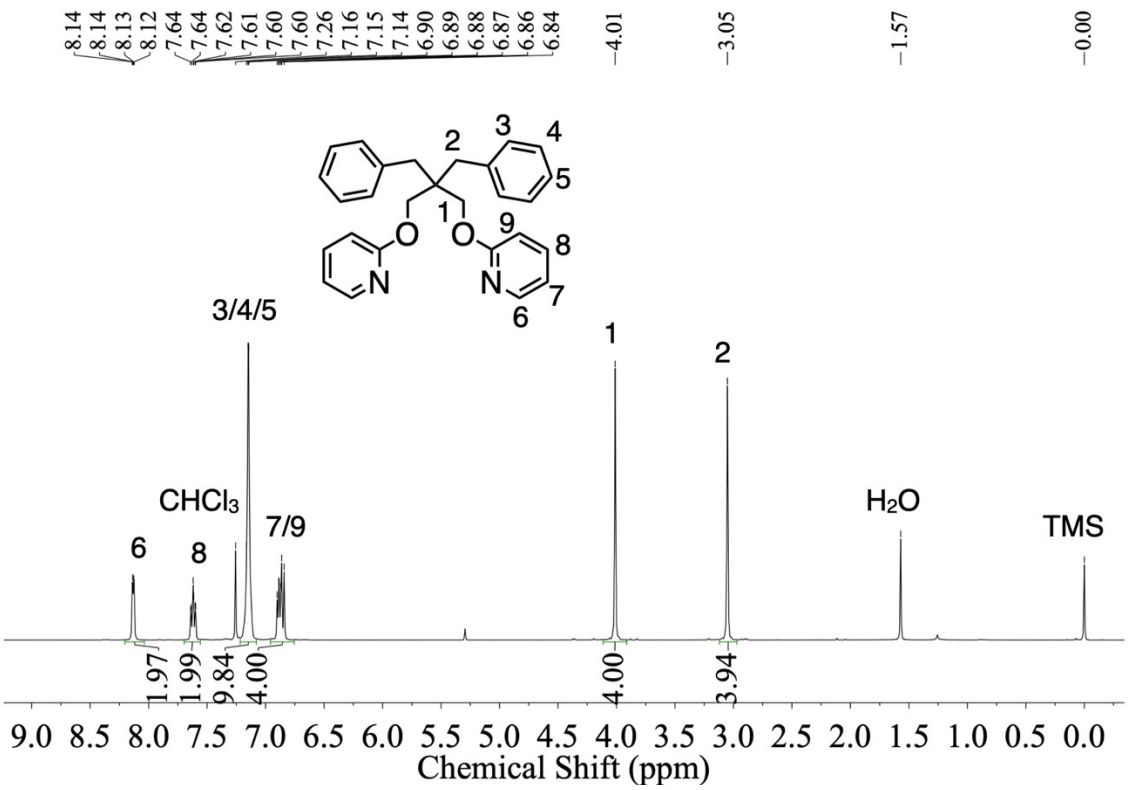

Figure S12. ^{1}H NMR (600MHz, $CDCl_3$) spectrum of precursor P1.

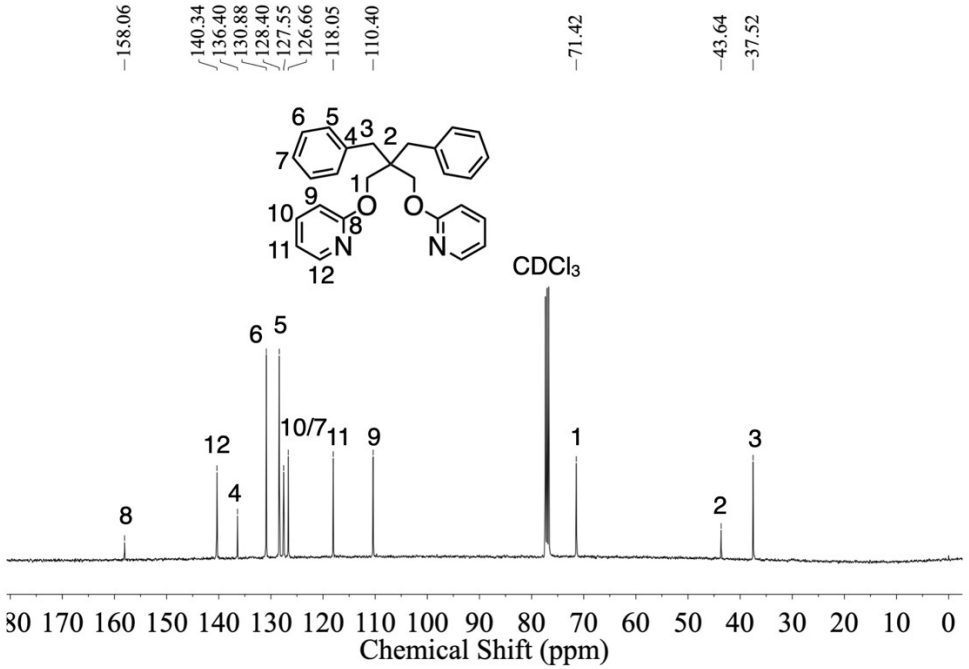

Figure S13. ^{13}C NMR (151 MHz, $CDCl_3$) spectrum of precursor P1.

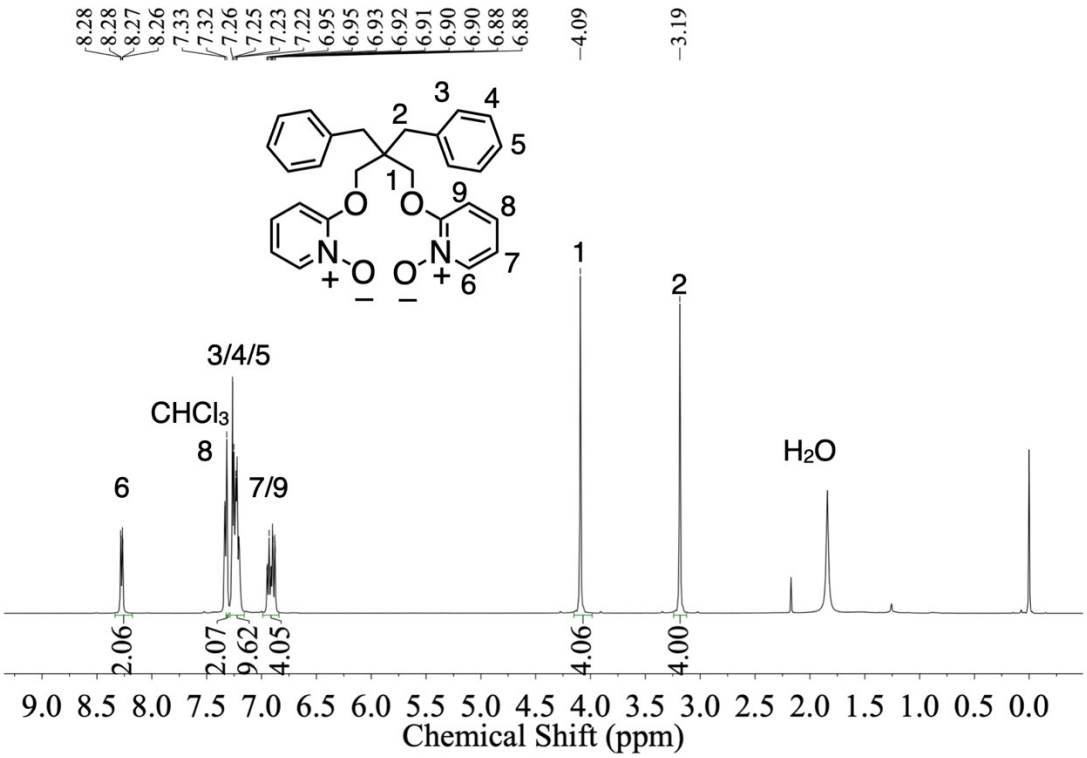

Figure S14. ^{1}H NMR (600MHz, $CDCl_3$) spectrum of precursor I5.

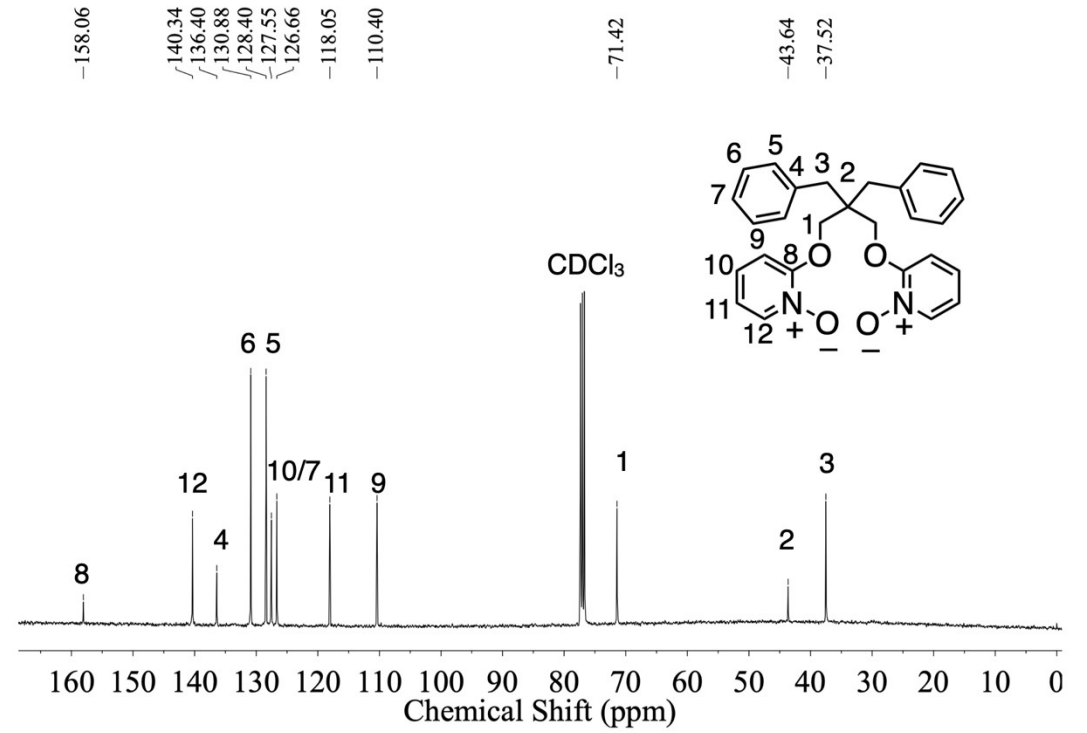

Figure S15. ^{13}C NMR (151 MHz, $CDCl_3$) spectrum of precursor I5.

Binding Analysis Using ^{1}H NMR Titration and 2D NMR Spectroscopy.

^{1}H NMR titrations in CD_3CN were conducted at 298 K on a Varian Unity Inova 400 MHz system with a cryoprobe. Aliquots from a stock solution containing the corresponding salts were added sequentially to an NMR tube containing a solution of the ionophores (600 μL). The ^{1}H NMR spectrum was acquired after each addition. The ^{1}H NMR titration spectra were analyzed by MestReNova software. The NMR titration isotherms were fitted[S4,S5] to a 1:1 host-guest binding model using Thordarson's equations at http://app.supramolecular.org/bindfit/. The data were then plotted using OriginLab software. The binding constants K_a were presented with standard deviations from the fitting outcomes.

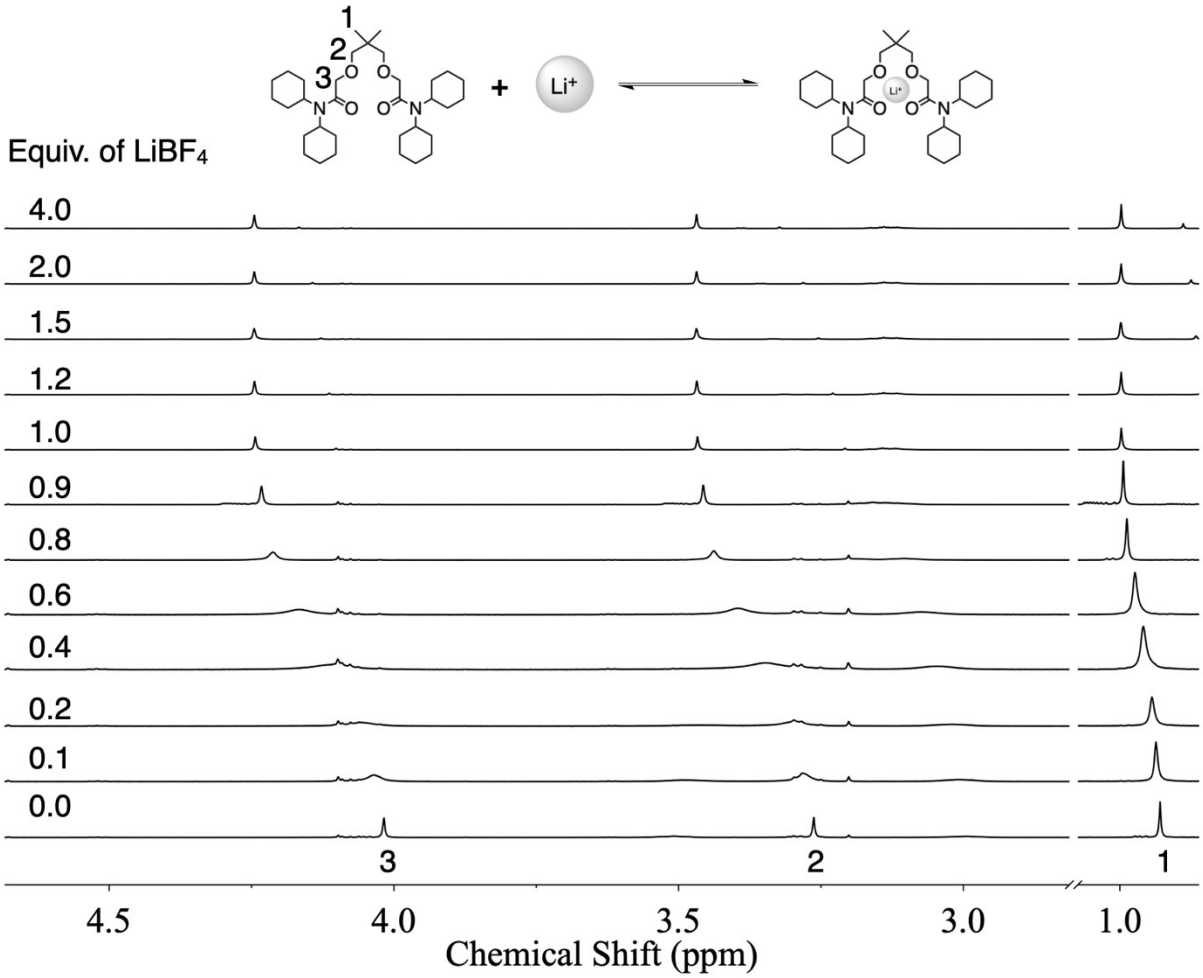

Figure S16. ^{1}H NMR spectra (500 MHz, CD_3CN, 298 K) of I1 (1.5 mM) titrated with $LiBF_4$.

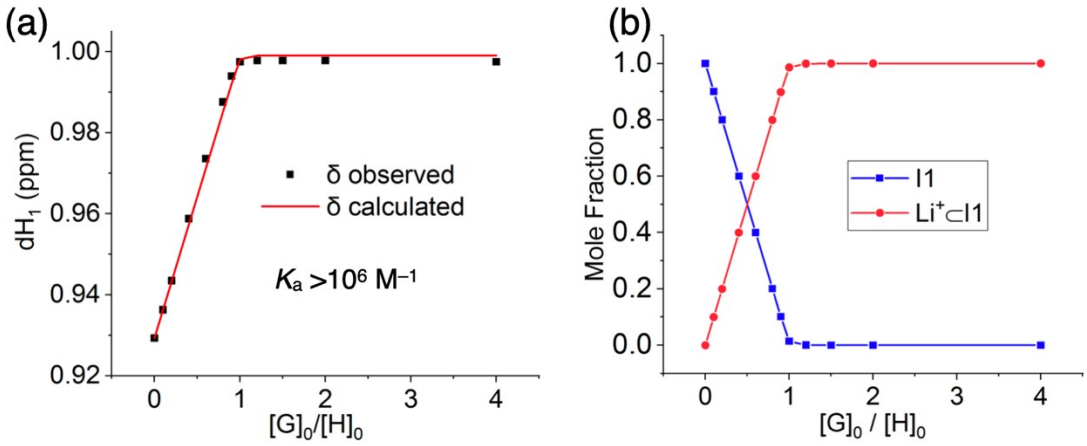

Figure S17. (a) Titration isotherm created by monitoring changes in the chemical shift of proton 1 for I1 (1.5 mM) caused by the addition of $LiBF_4$ in CD_3CN at 298 K. Red lines is the curve fitting using a 1:1 host-guest binding model. (b) Calculated changes of mole fractions for I1 (blue trace) and $Li^+ \subset$I1 (red trace) over the host-guest mole ratio.

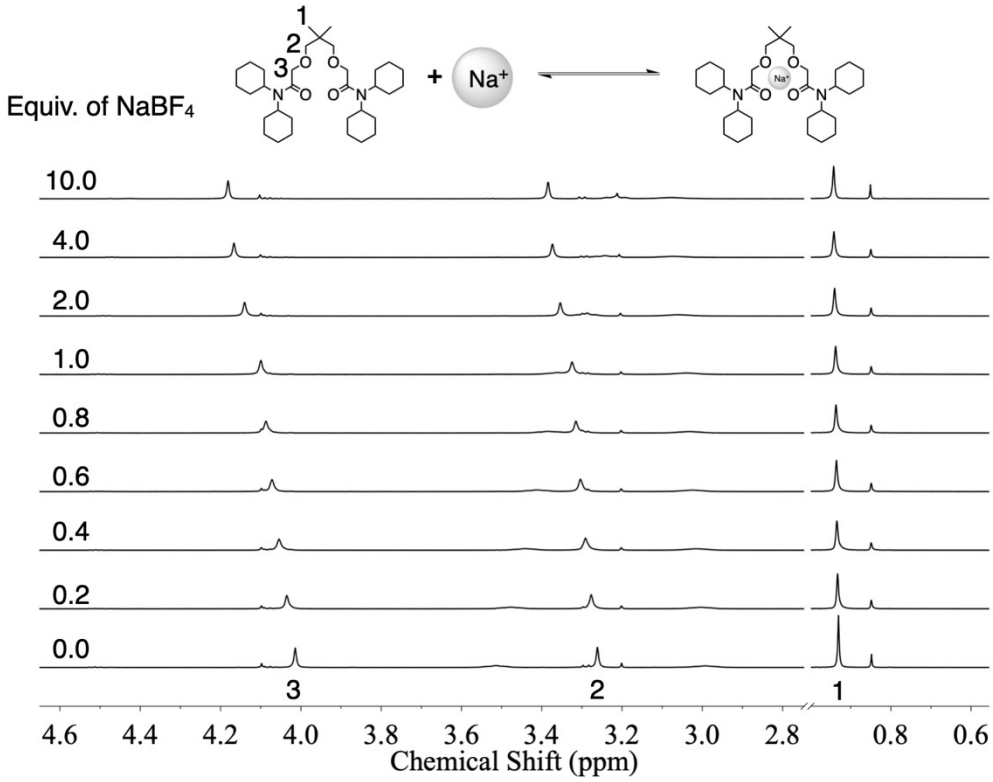

Figure S18. ^1H NMR spectra (500 MHz, CD_3CN, 298 K) of I1 (1.5 mM) titrated with $NaBF_4$.

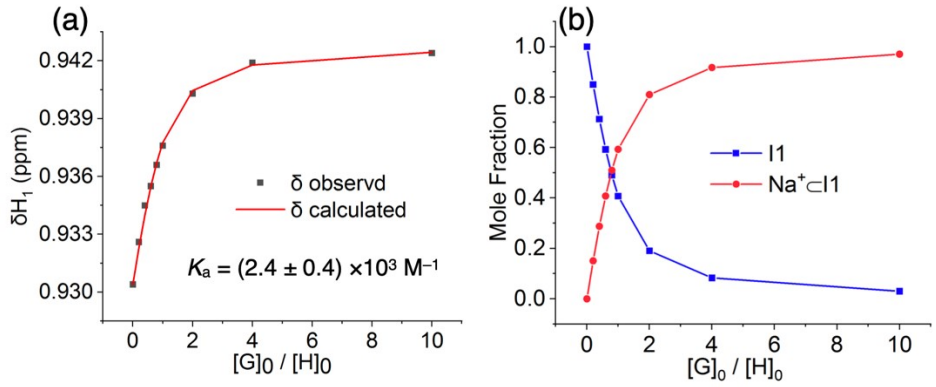

Figure S19. (a) Titration isotherm created by monitoring changes in the chemical shift of proton 1 for I1 (1.5 mM) caused by the addition of $NaBF_4$ in CD_3CN at 298 K. Red lines is the curve fitting using a 1:1 host-guest binding model. (b) Calculated changes of mole fractions for I1 (blue trace) and $Na^+\subset$I1 (red trace) over the host-guest mole ratio.

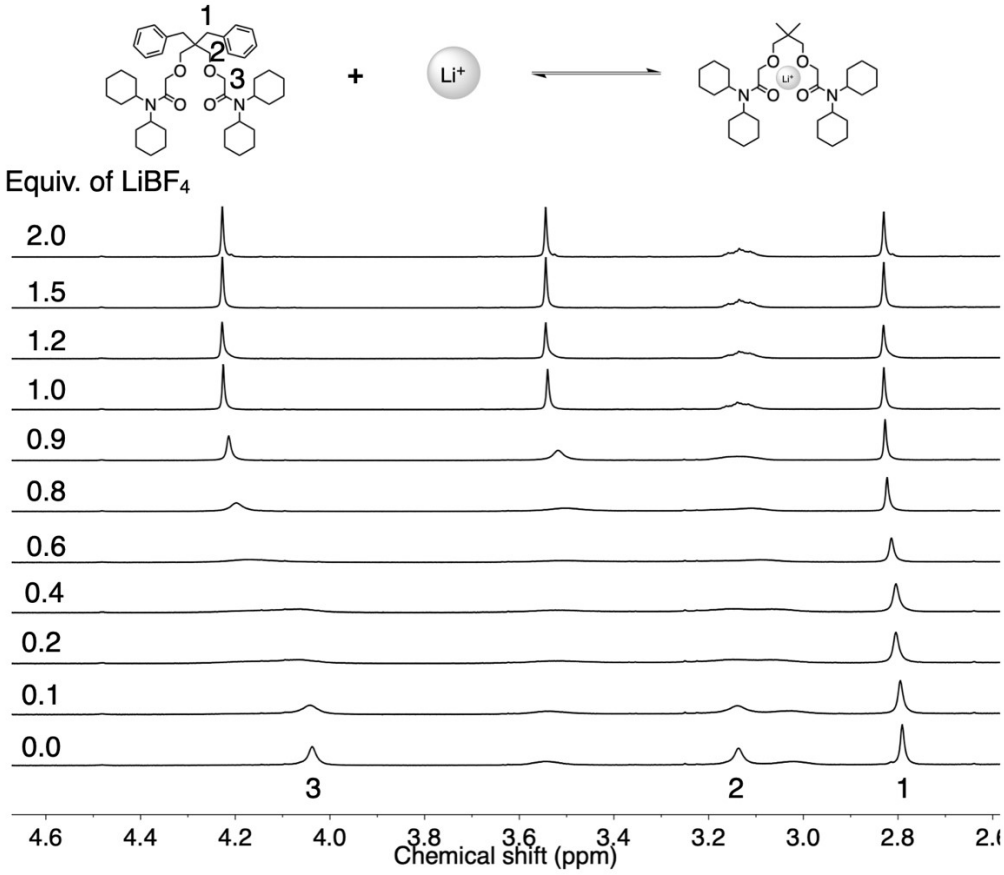

Figure S20. Figure S11. ^{1}H NMR spectra (500 MHz, CD_3CN, 298 K) of I2 (1.5 mM) titrated with $LiBF_4$.

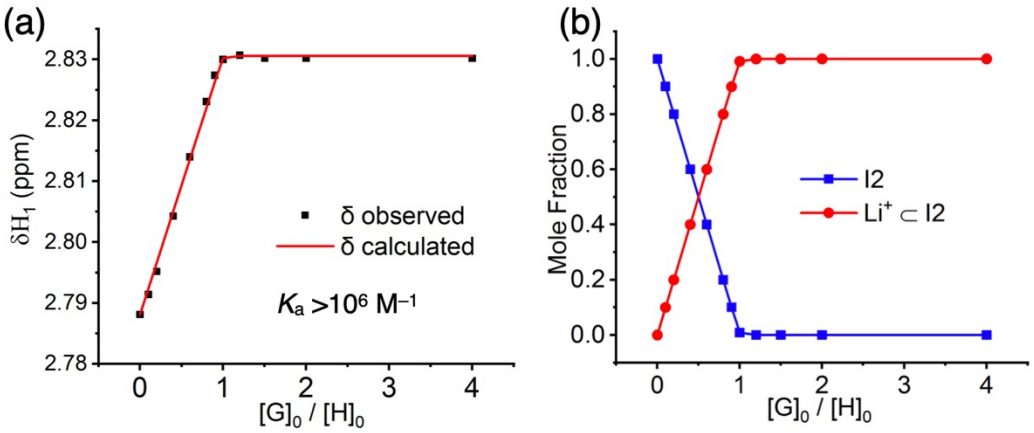

Figure S21. (a) Titration isotherm created by monitoring changes in the chemical shift of proton 1 for I2 (1.5 mM) caused by the addition of $LiBF_4$ in CD_3CN at 298 K. Red lines is the curve fitting using a 1:1 host-guest binding model. (b) Calculated changes of mole fractions for I2 (blue trace) and $Li^+ \subset$ I2 (red trace) over the host-guest mole ratio.

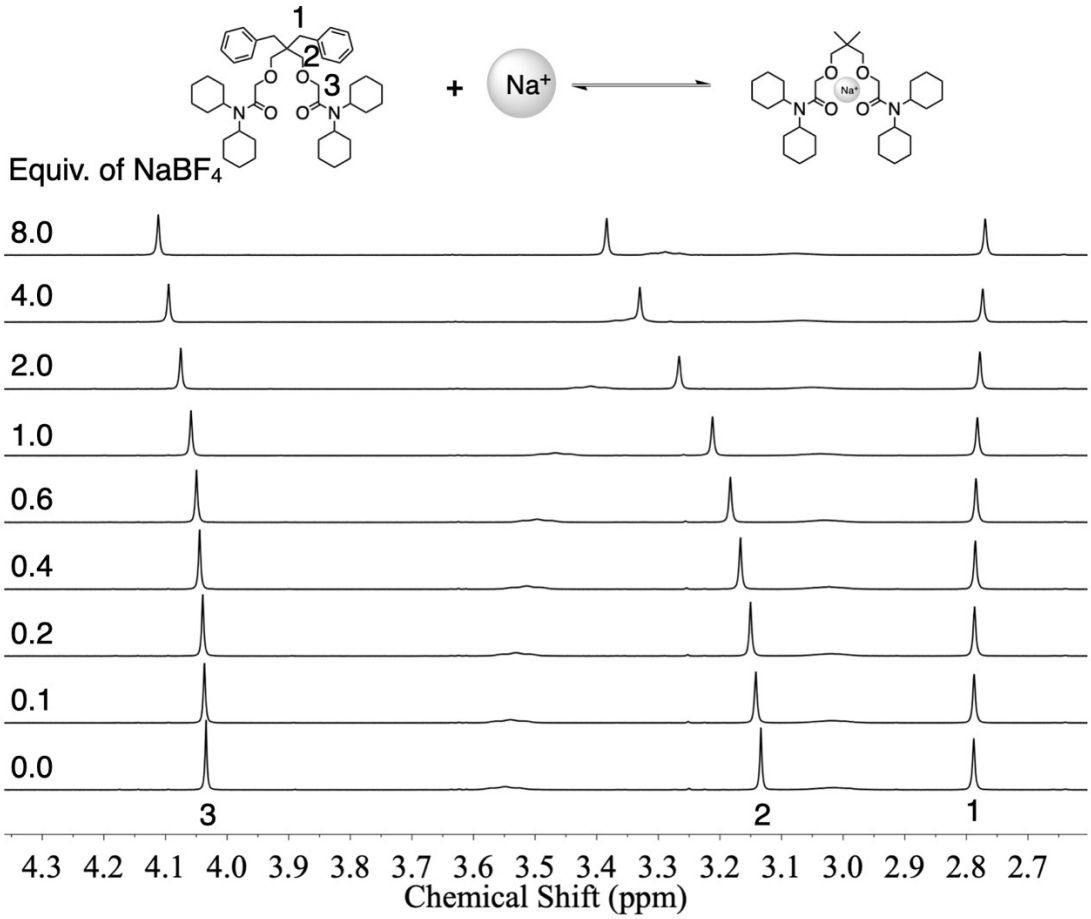

Figure S22. ^1H NMR spectra (500 MHz, CD_3CN, 298 K) of I2 (1.5 mM) titrated with $NaBF_4$.

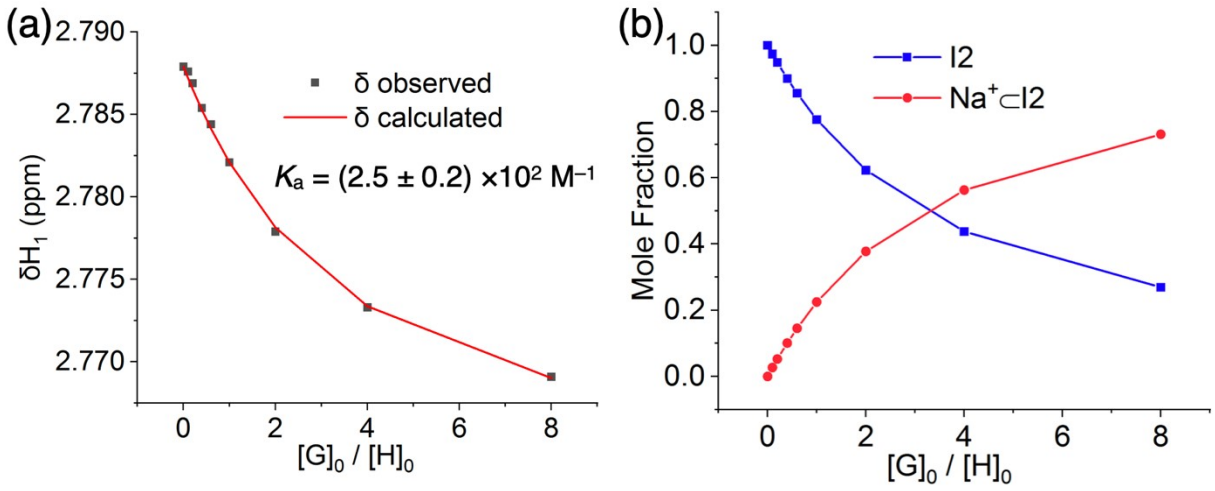

Figure S23. (a) Titration isotherm created by monitoring changes in the chemical shift of proton 1 for I2 (1.5 mM) caused by the addition of $NaBF_4$ in CD_3CN at 298 K. Red lines is the curve fitting using a 1:1 host-guest binding model. (b) Calculated changes of mole fractions for I2 (blue trace) and $Na^+\subset$I2 (red trace) over the host-guest mole ratio.

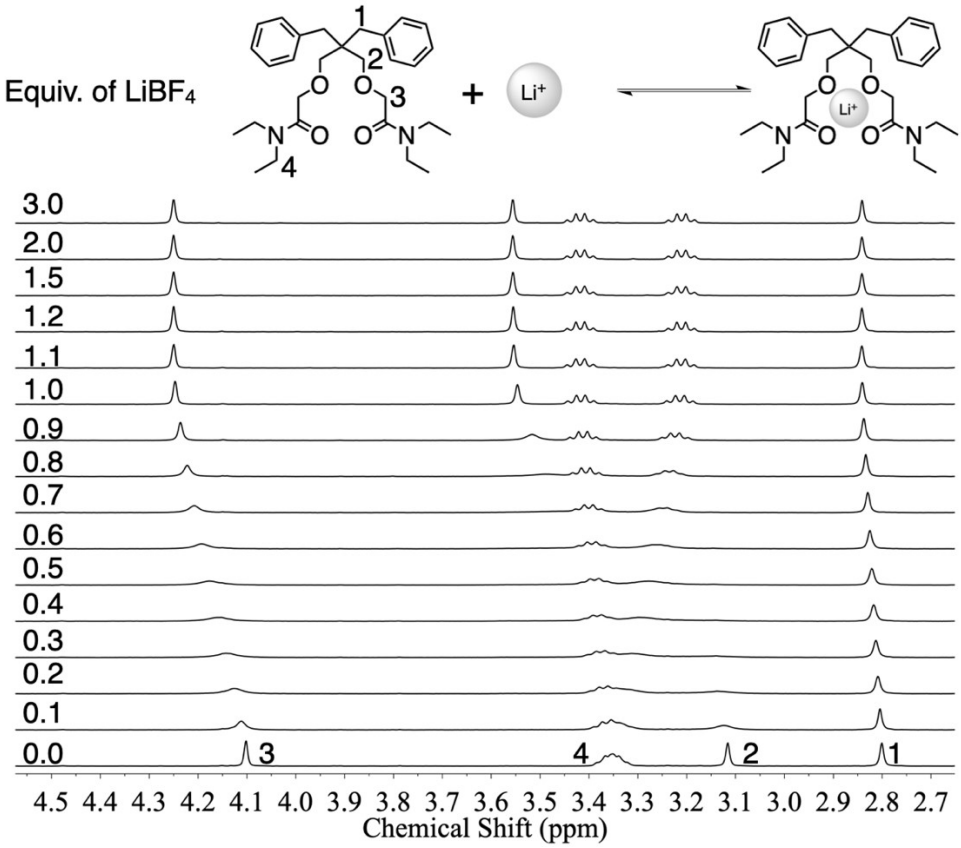

Figure S24. ^{1}H NMR spectra (500 MHz, CD_3CN, 298 K) of I3 (1.0 mM) titrated with $LiBF_4$.

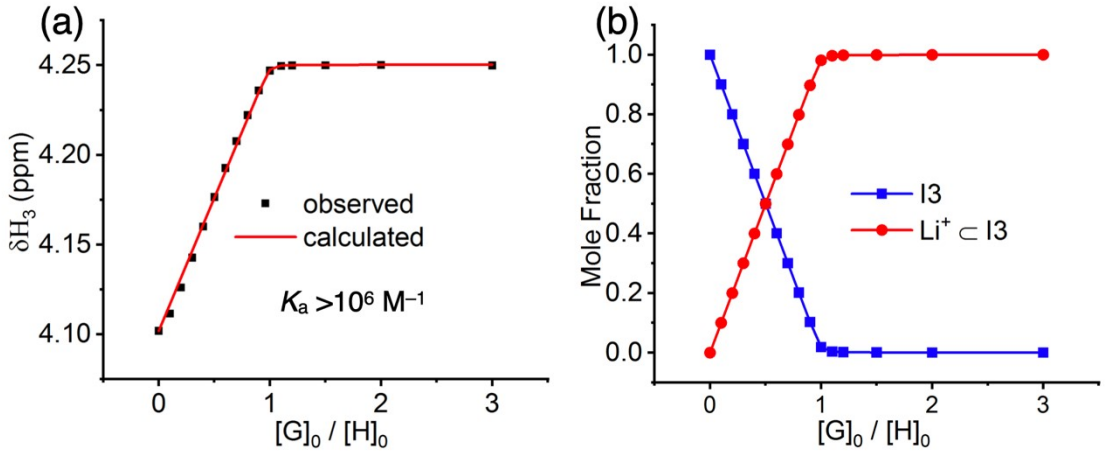

Figure S25. (a) Titration isotherm created by monitoring changes in the chemical shift of proton 3 for I3 (1.0 mM) caused by the addition of $LiBF_4$ in CD_3CN at 298 K. Red lines is the curve fitting using a 1:1 host-guest binding model. (b) Calculated changes of mole fractions for I3 (blue trace) and $Li^+ \subset$ I3 (red trace) over the host-guest mole ratio.

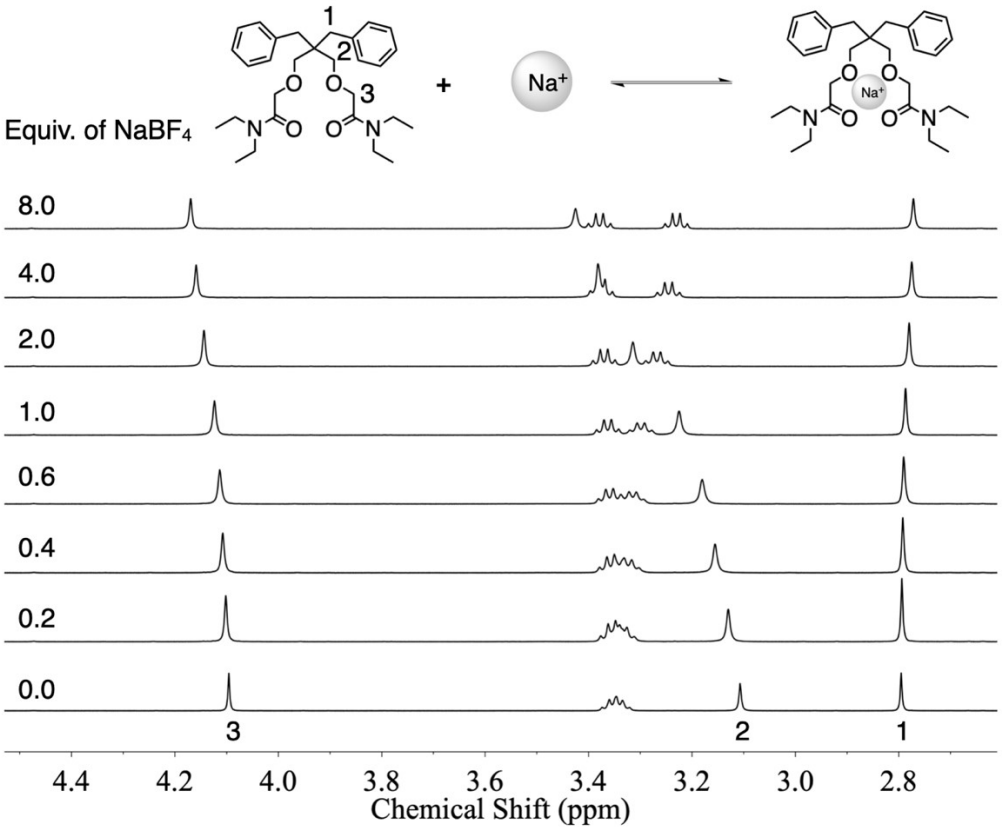

Figure S26. ^1H NMR spectra (500 MHz, CD_3CN, 298 K) of I3 (1.5 mM) titrated with $NaBF_4$.

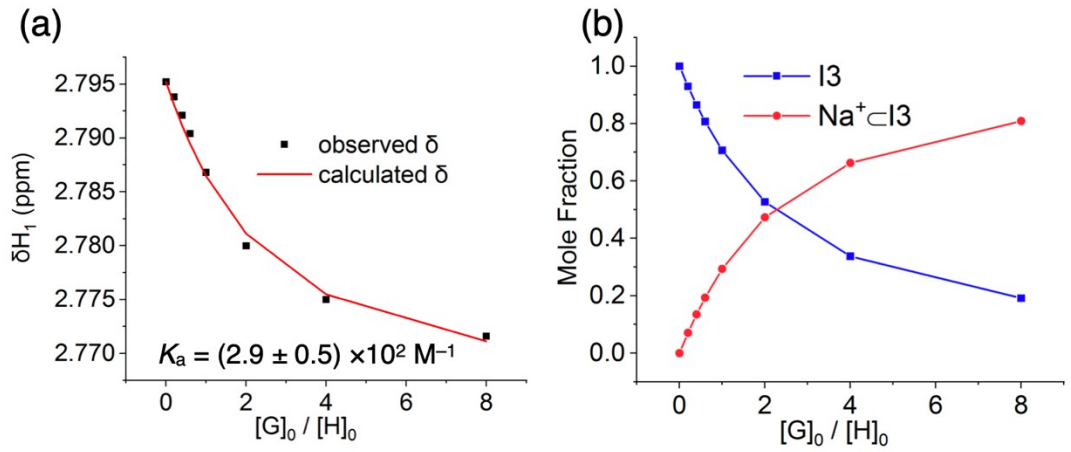

Figure S27. (a) Titration isotherm created by monitoring changes in the chemical shift of proton 1 for I3 (1.5 mM) caused by the addition of $NaBF_4$ in CD_3CN at 298 K. Red lines is the curve fitting using a 1:1 host-guest binding model. (b) Calculated changes of mole fractions for I3 (blue trace) and $Na^+\subset$I3 (red trace) over the host-guest mole ratio.

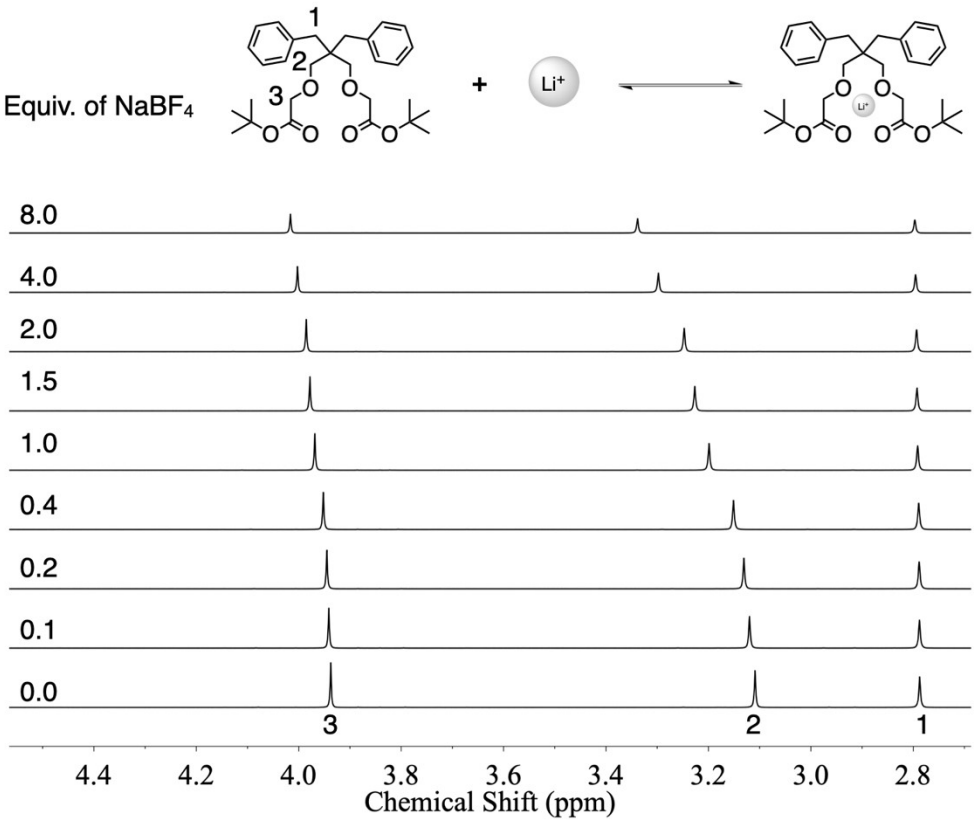

Figure S28. ^{1}H NMR spectra (500 MHz, CD_3CN, 298 K) of I4 (5.0 mM) titrated with $LiBF_4$.

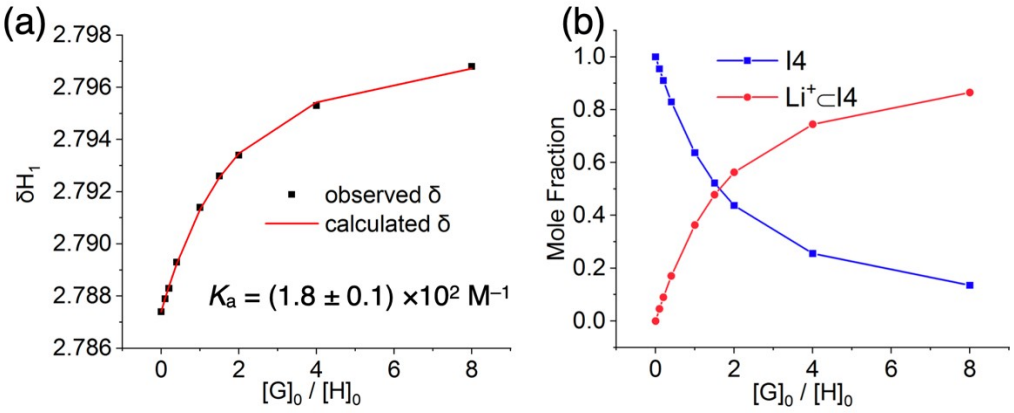

Figure S29. (a) Titration isotherm created by monitoring changes in the chemical shift of proton 1 for I4 (5 mM) caused by the addition of $NaBF_4$ in CD_3CN at 298 K. Red lines is the curve fitting using a 1:1 host-guest binding model. (b) Calculated changes of mole fractions for I4 (blue trace) and $Li^+\subset$I4 (red trace) over the host-guest mole ratio.

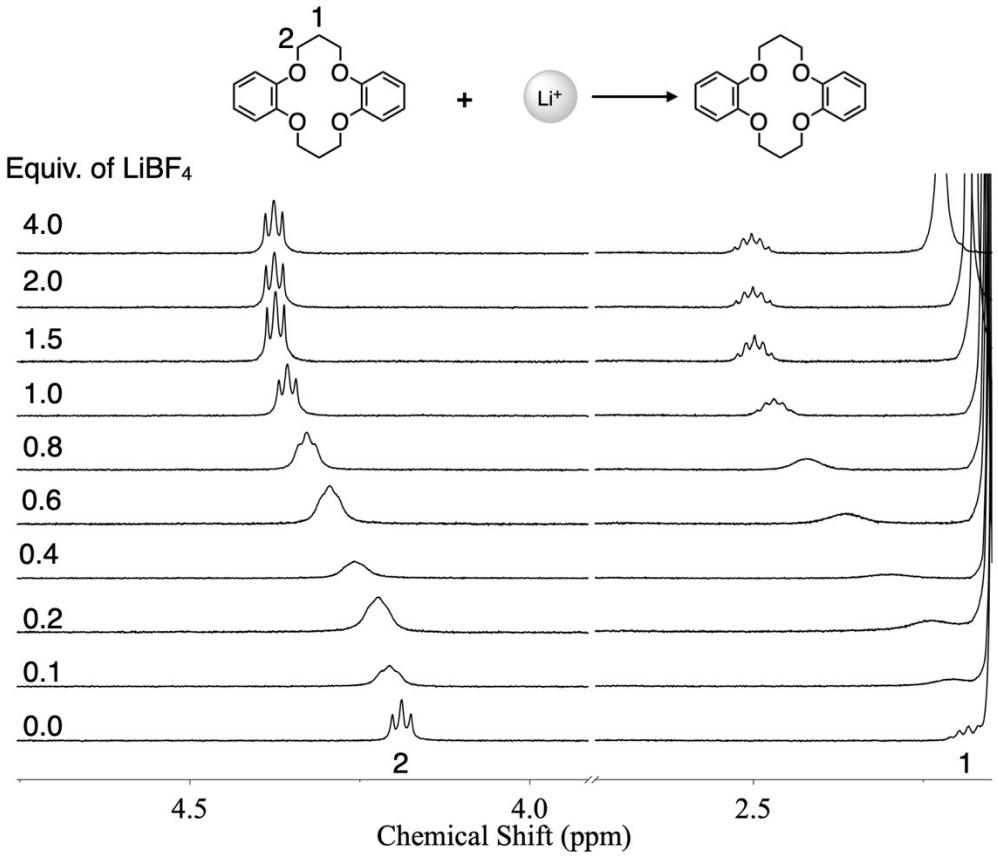

Figure S30. ^{1}H NMR spectra (500 MHz, CD_3CN, 298 K) of DB-14-C-4 (2.0 mM) titrated with $LiBF_4$.

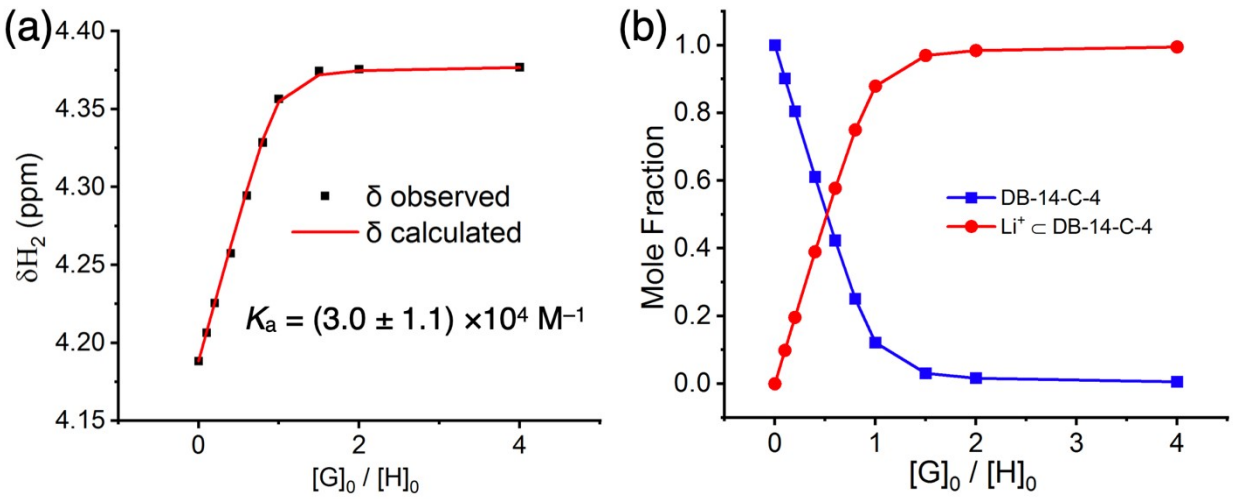

Figure S31. (a) Titration isotherm created by monitoring changes in the chemical shift of proton 1 for DB-14-C-4 (2.0 mM) caused by the addition of $NaBF_4$ in CD_3CN at 298 K. Red lines is the curve fitting using a 1:1 host-guest binding model. (b) Calculated changes of mole fractions for DB-14-C-4 (blue trace) and Li^+⊂DB-14-C-4 (red trace) over the host-guest mole ratio.

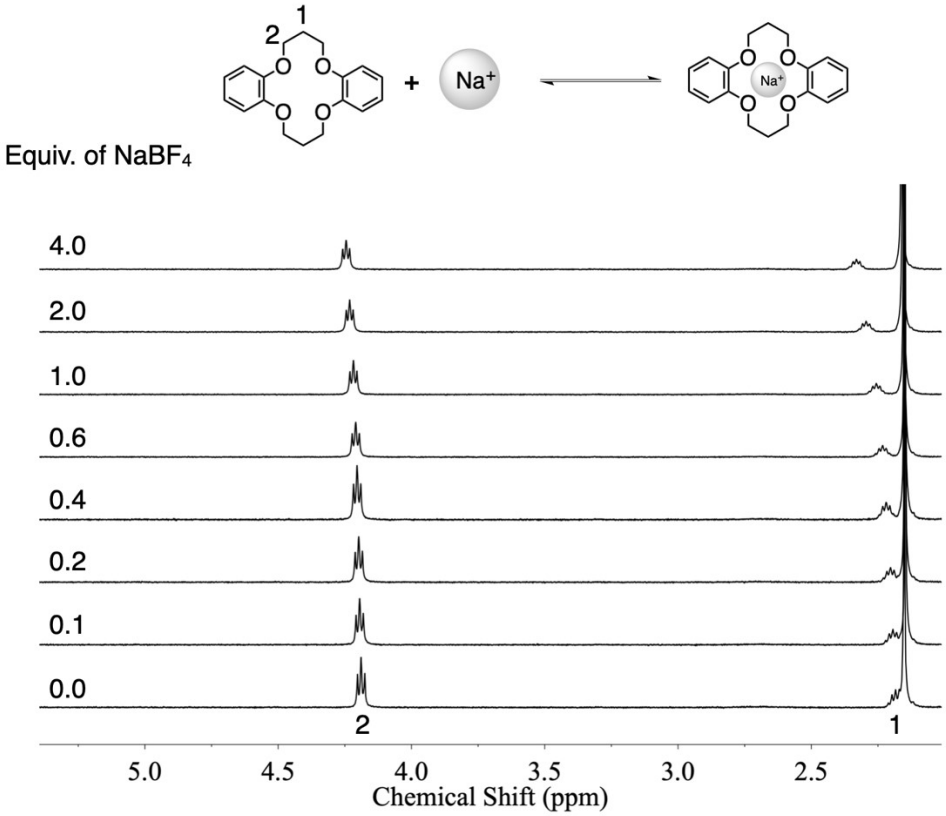

Figure S32. ^1H NMR spectra (500 MHz, CD_3CN, 298 K) of DB-14-C-4 (2.0 mM) titrated with $NaBF_4$.

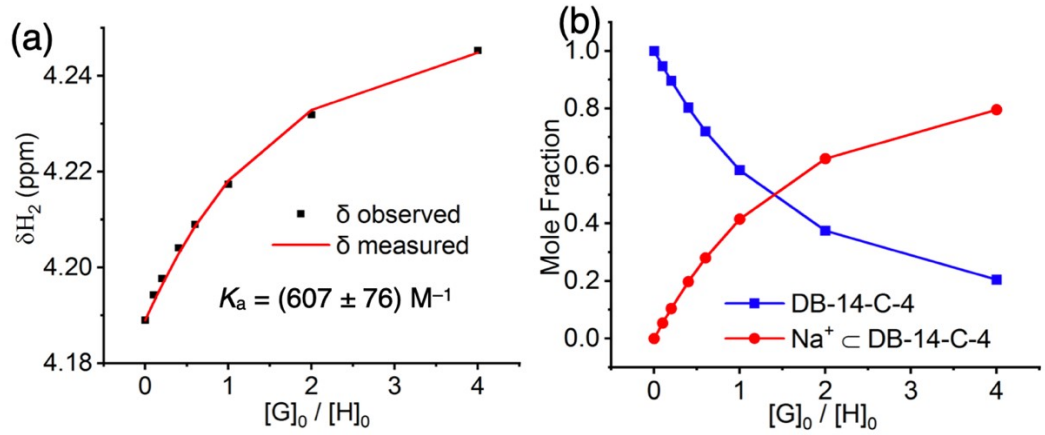

Figure S33. (a) Titration isotherm created by monitoring changes in the chemical shift of proton 1 for DB-14-C-4 (2 mM) caused by the addition of $NaBF_4$ in CD_3CN at 298 K. Red lines is the curve fitting using a 1:1 host-guest binding model. (b) Calculated changes of mole fractions for DB-14-c-4 (blue trace) and Na^+⊂DB-14-C-4 (red trace) over the host-guest mole ratio.

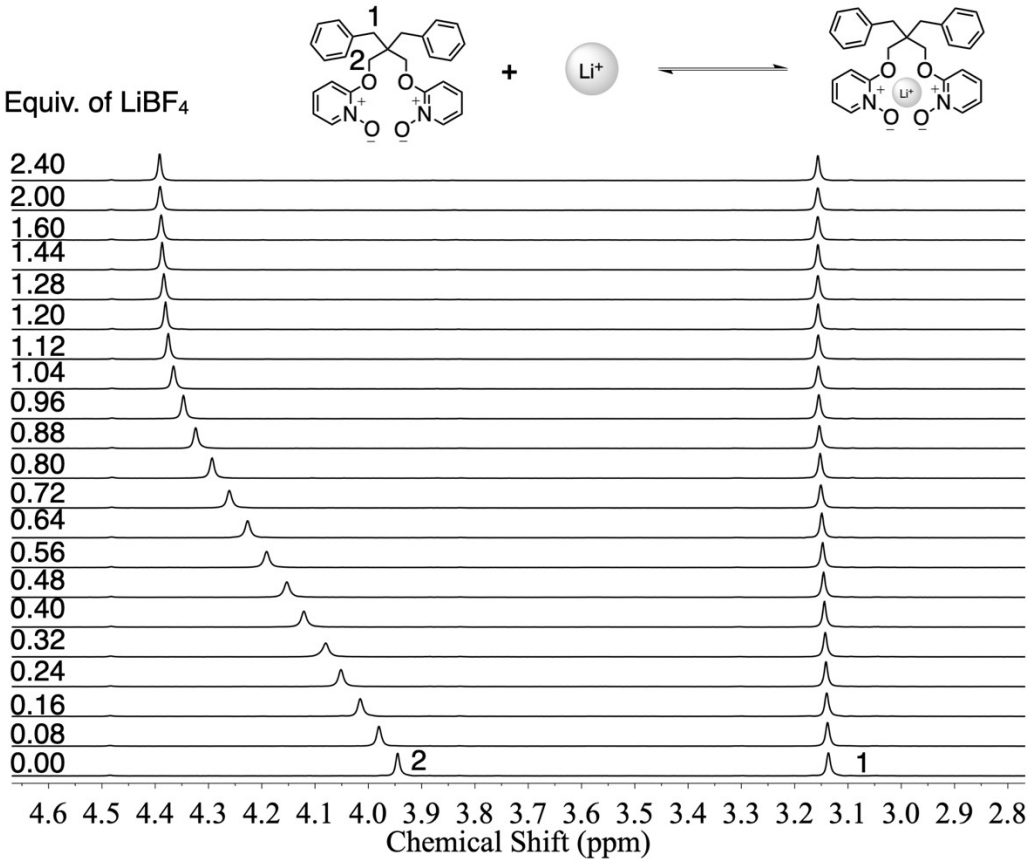

Figure S34. ^1H NMR spectra (500 MHz, CD_3CN, 298 K) of I5 (1.25 mM) titrated with $LiBF_4$.

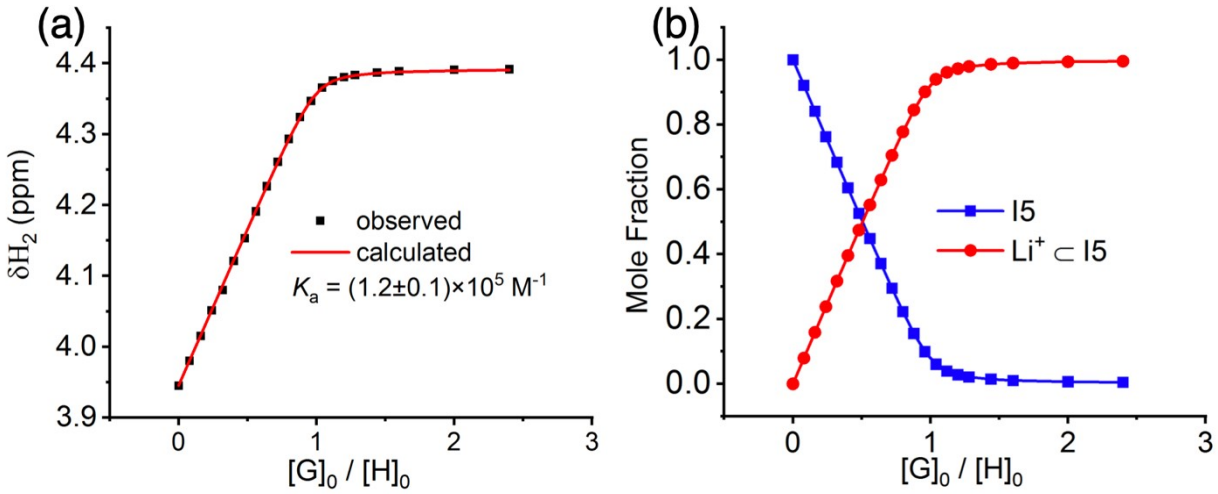

Figure S35. (a) Titration isotherm created by monitoring changes in the chemical shift of proton 2 for I5 (1.25 mM) caused by the addition of $LiBF_4$ in CD_3CN at 298 K. Red lines is the curve fitting using a 1:1 host-guest binding model. (b) Calculated changes of mole fractions for I5 (blue trace) and $Li^+ \subset$I5 (red trace) over the host-guest mole ratio.

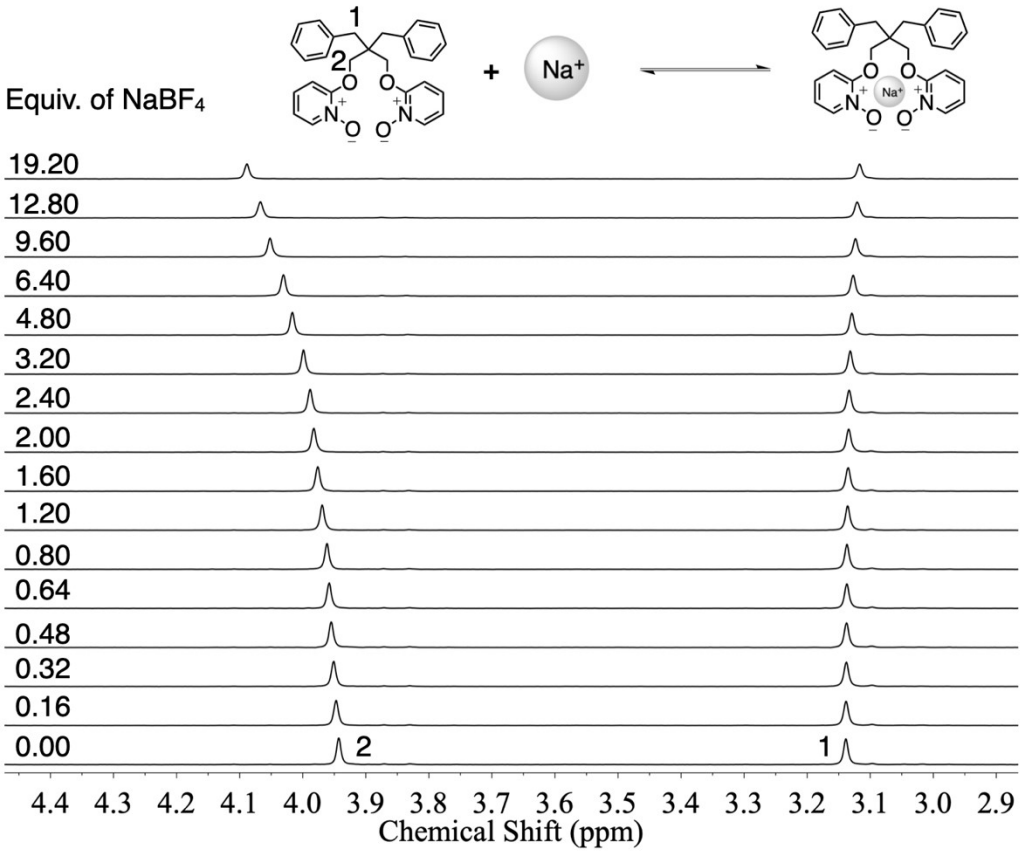

Figure S36. ^1H NMR spectra (500 MHz, CD_3CN, 298 K) of I5 (1.25 mM) titrated with $NaBF_4$.

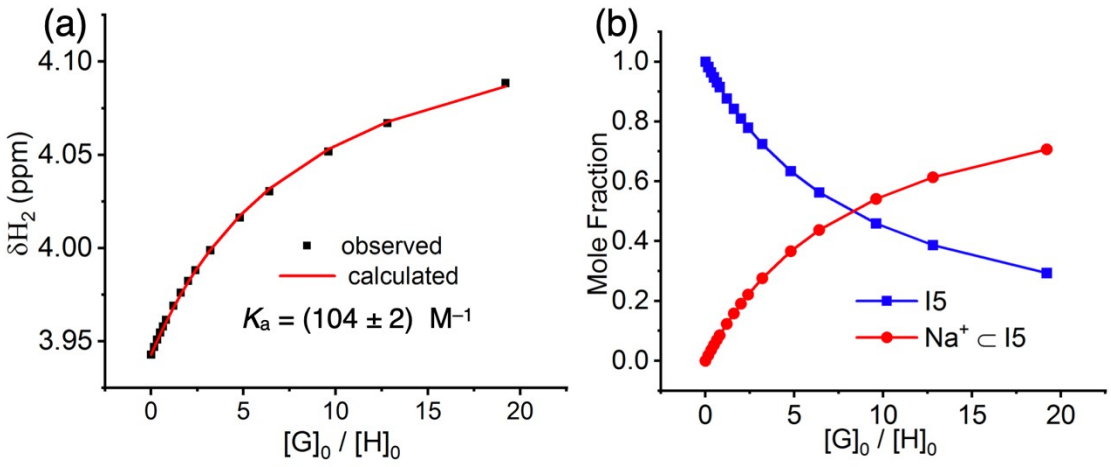

Figure S37. (a) Titration isotherm created by monitoring changes in the chemical shift of proton 2 for I5 (1.25 mM) caused by the addition of $NaBF_4$ in CD_3CN at 298 K. Red lines is the curve fitting using a 1:1 host-guest binding model. (b) Calculated changes of mole fractions for I5 (blue trace) and $Na^+ \subset$I5 (red trace) over the host-guest mole ratio.

5. Isothermal Titration Calorimetry

Isothermal titration was performed on the MicroCal iTC_{200} system at 23 °C. The experiments were conducted in the 200 μL working volume of the sample cell. The capacity of the injection syringe is 40 μL. The stirring speed was set at 750 rpm. Host and guest solutions were prepared in MeCN. A host solution was placed in the titration cell, and the guests were loaded into the titration syringe. In each case, 20-25 injections were performed. The heat of dilution was measured by titrating the guest into a blank solution. The heat of dilution was subtracted before analyzing with MicroCal iTC_{200} software using a 1:1 host-guest binding model and plotted by Origin Lab software. Note: A small endothermic peak was observed at the end of each titration. This artifact is caused by the heat of dilution when a highly concentrated salt solution is diluted to MeCN. This non-binding signal is subtracted during the data fitting process and has no impact on the interpretation of the results.

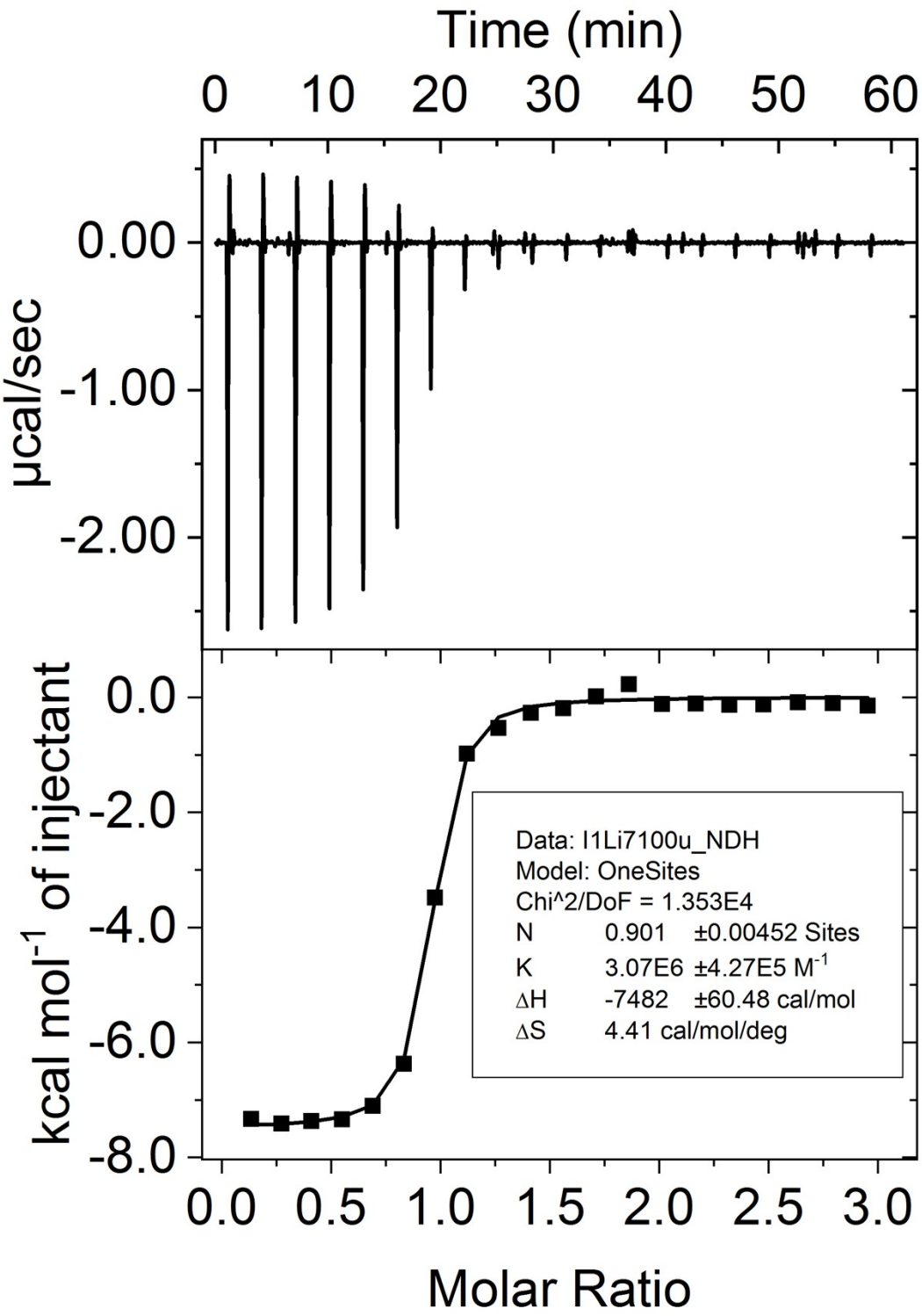

Figure S38. ITC profiles for the titration of I1 (0.07mM in the cell) with $LiBF_4$ (1.0 mM in syringe) in MeCN. The solid line represents the best non-linear fit of the data to a 1:1 binding model.

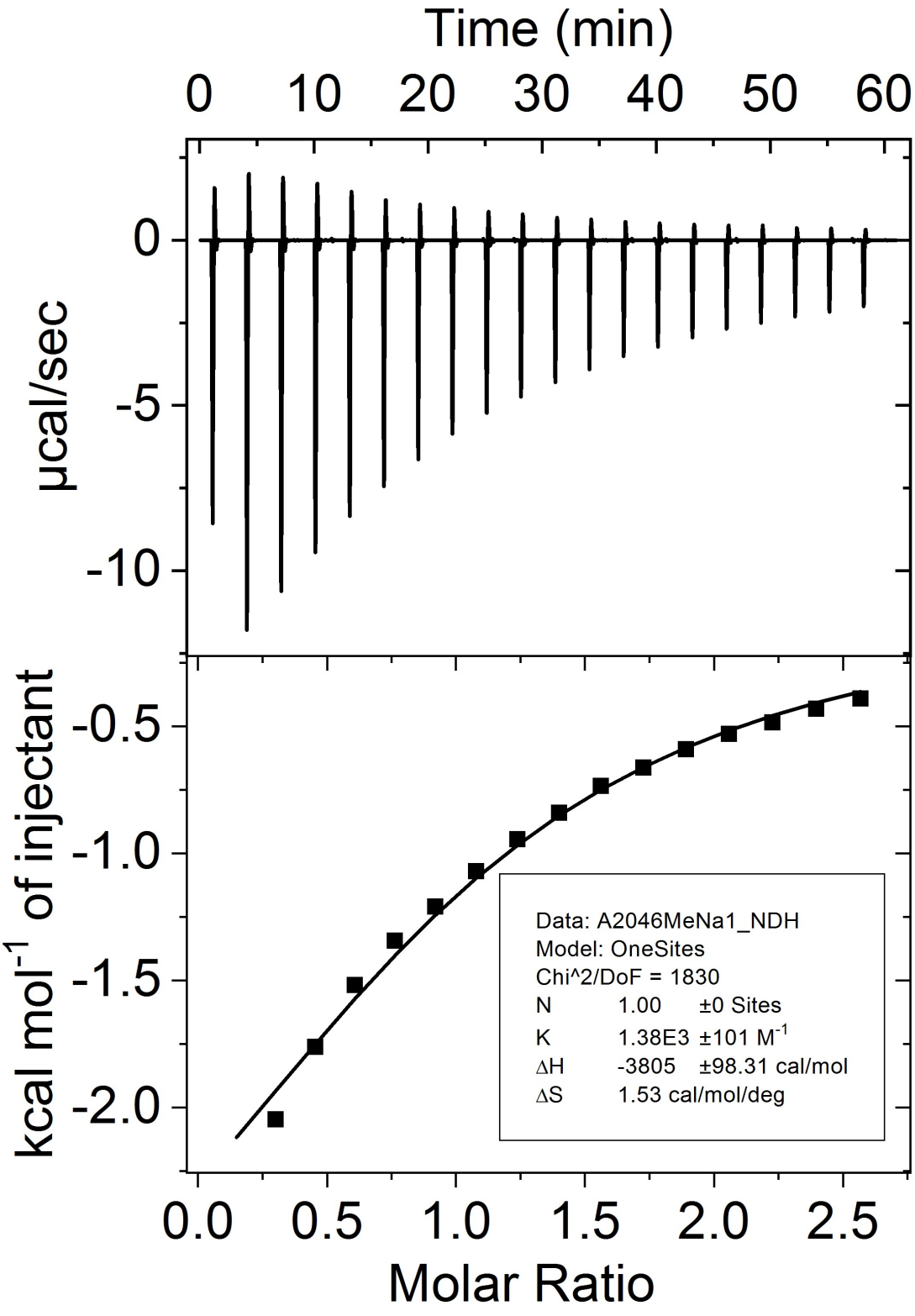
Time (min)
0
10
20
30
40
50
60
0
-5
-10
µcal/sec
-0.5
-1.0
-1.5
-2.0
kcal mol-1 of injectant
Data: A2046MeNa1_NDH
Model: OneSites
Chi^2/DoF = 1830
N 1.00 ±0 Sites
K 1.38E3 ±101 M-1
ΔH -3805 ±98.31 cal/mol
ΔS 1.53 cal/mol/deg
0.0
0.5
1.0
1.5
2.0
2.5
Molar Ratio

Figure S39. ITC profiles for the titration of I1 (1.0 mM in the cell) with $NaBF_4$ (15.8 mM in syringe) in MeCN. The solid line represents the best non-linear fit of the data to a 1:1 binding model.

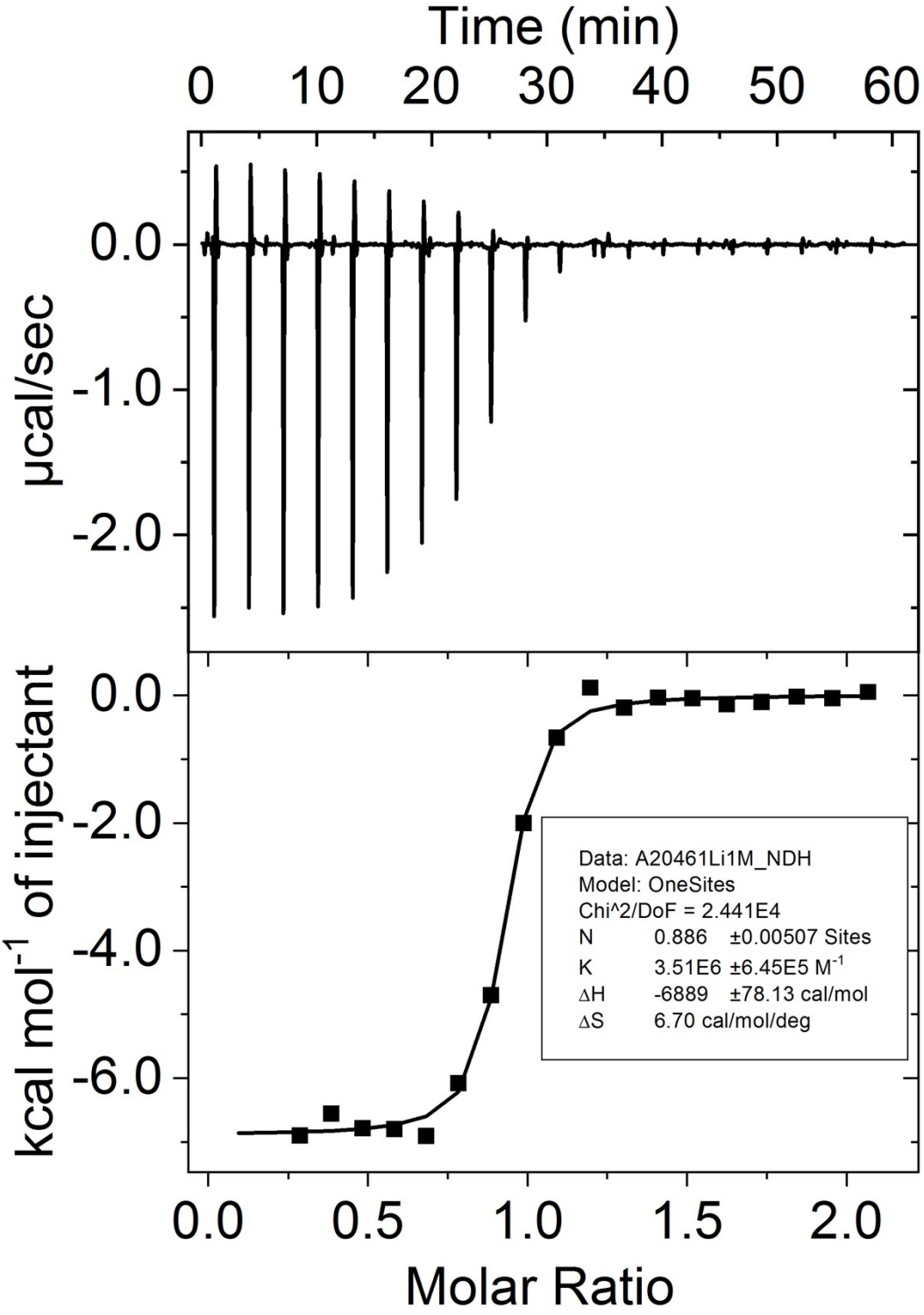

Figure S40. ITC profiles for the titration of I2 (0.1 mM in the cell) with $LiBF_4$ (1.0 mM in syringe) in MeCN. The solid line represents the best non-linear fit of the data to a 1:1 binding model.

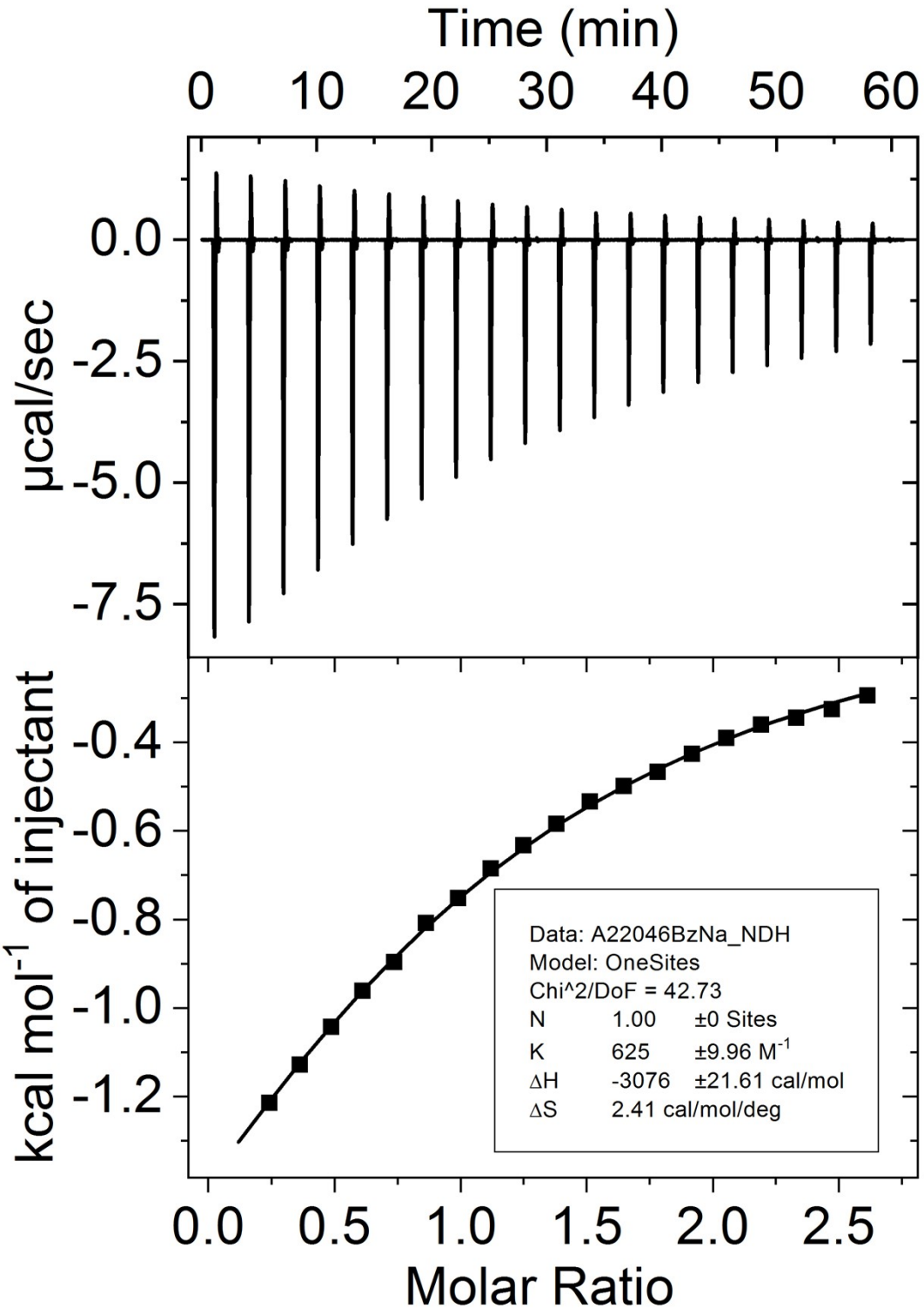

Figure S41. ITC profiles for the titration of I2 (1.2 mM in the cell) with $NaBF_4$ (15.8 mM in syringe) in MeCN. The solid line represents the best non-linear fit of the data to a 1:1 binding model.

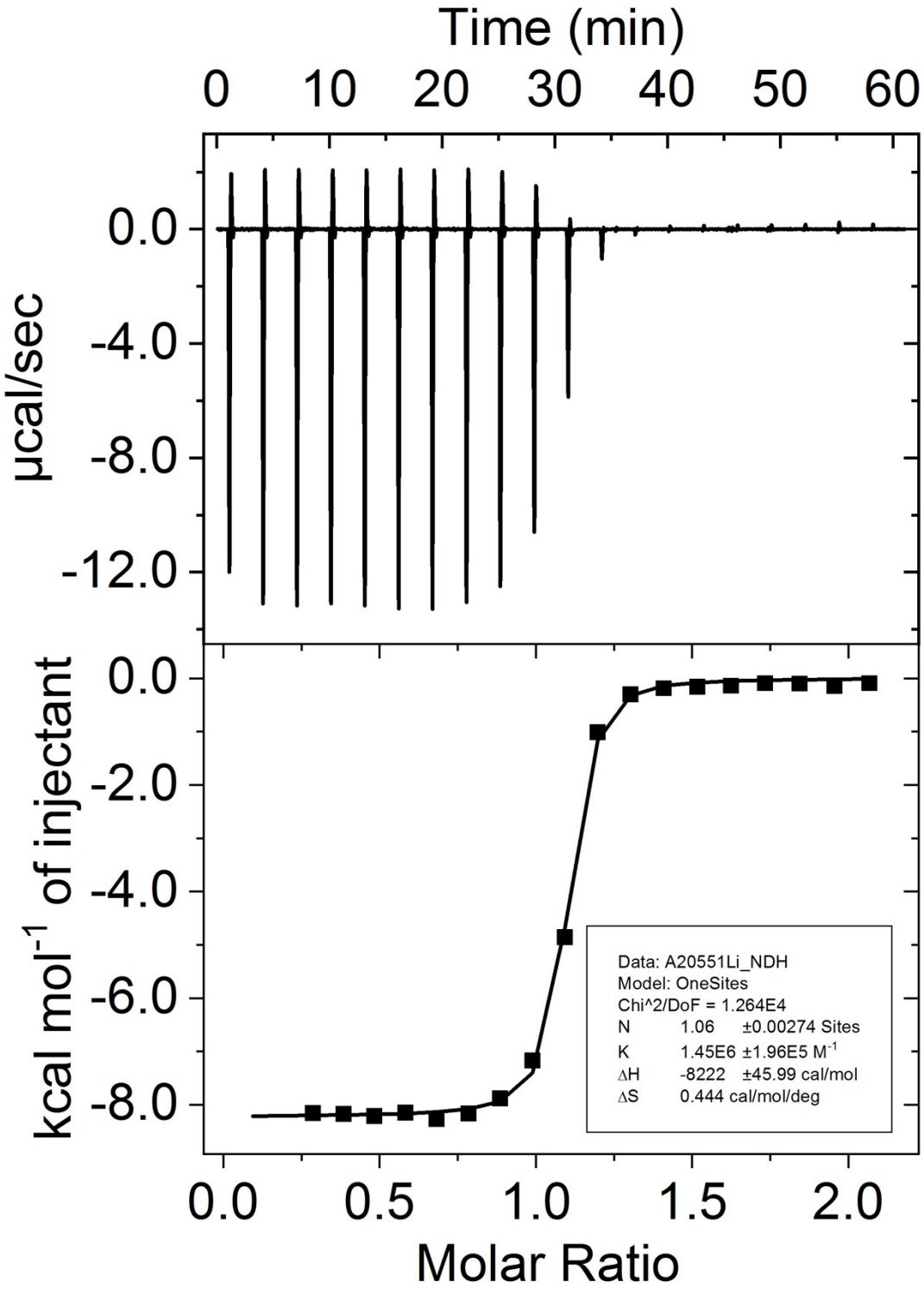

Figure S42. ITC profiles for the titration of I3 (0.5 mM in the cell) with $LiBF_4$ (5.0 mM in syringe) in MeCN. The solid line represents the best non-linear fit of the data to a 1:1 binding model.

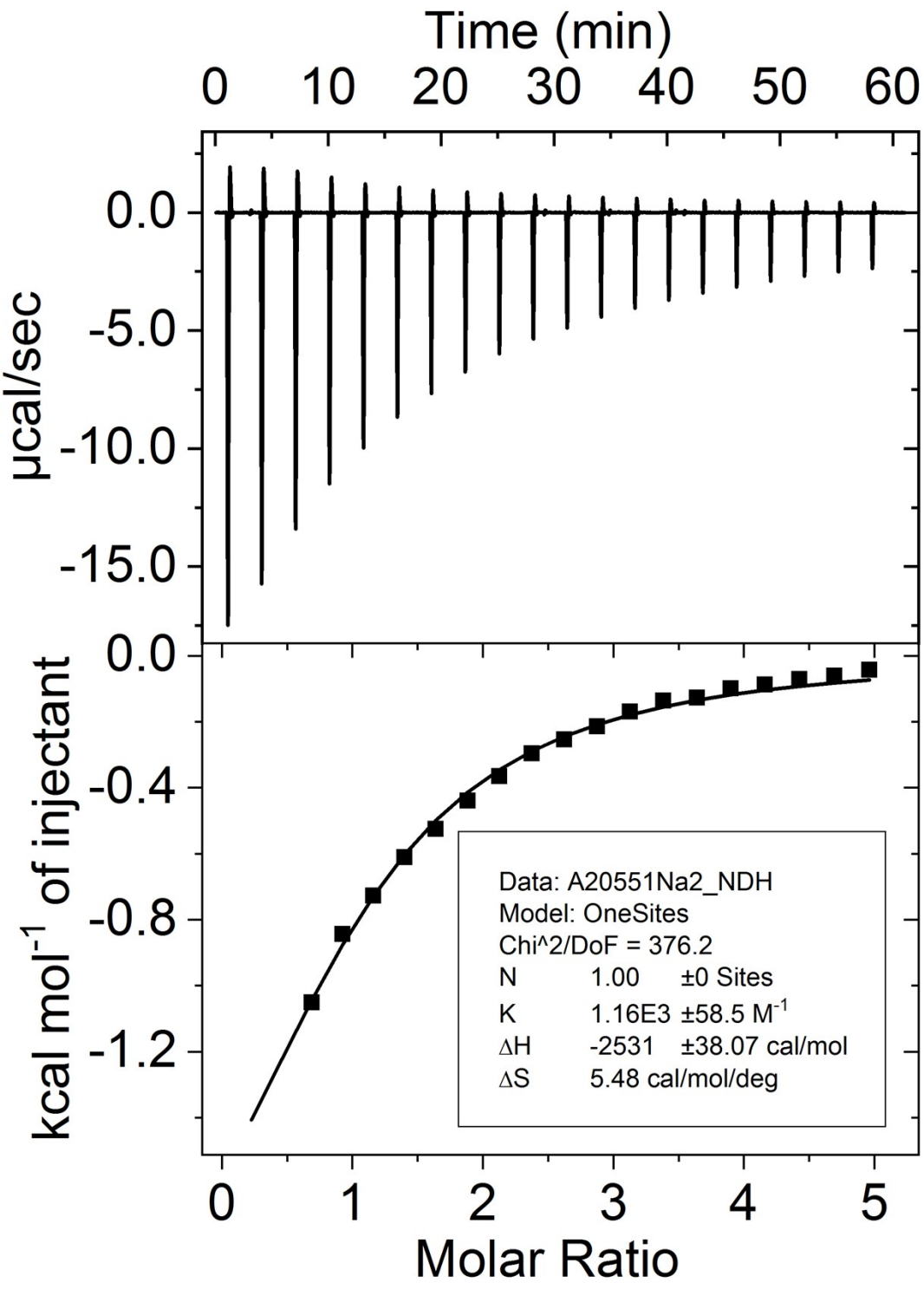

Figure S43. ITC profiles for the titration of I3 (1.2 mM in the cell) with $NaBF_4$ (30.0 mM in syringe) in MeCN. The solid line represents the best non-linear fit of the data to a 1:1 binding model.

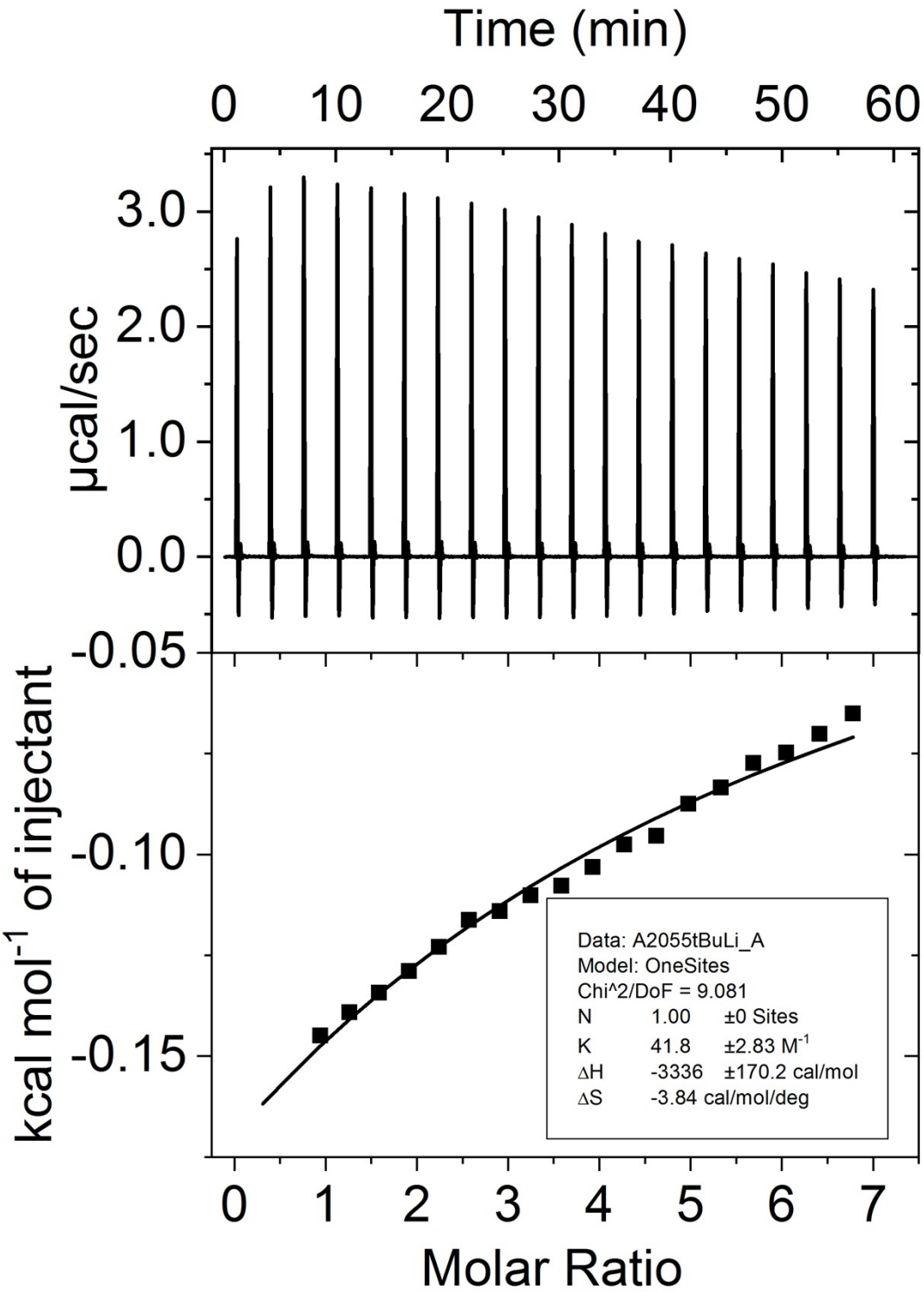

Figure S44. ITC profiles for the titration of I4 (1.2 mM in the cell) with $LiBF_4$ (41.0 mM in syringe) in MeCN. The solid line represents the best non-linear fit of the data to a 1:1 binding model.

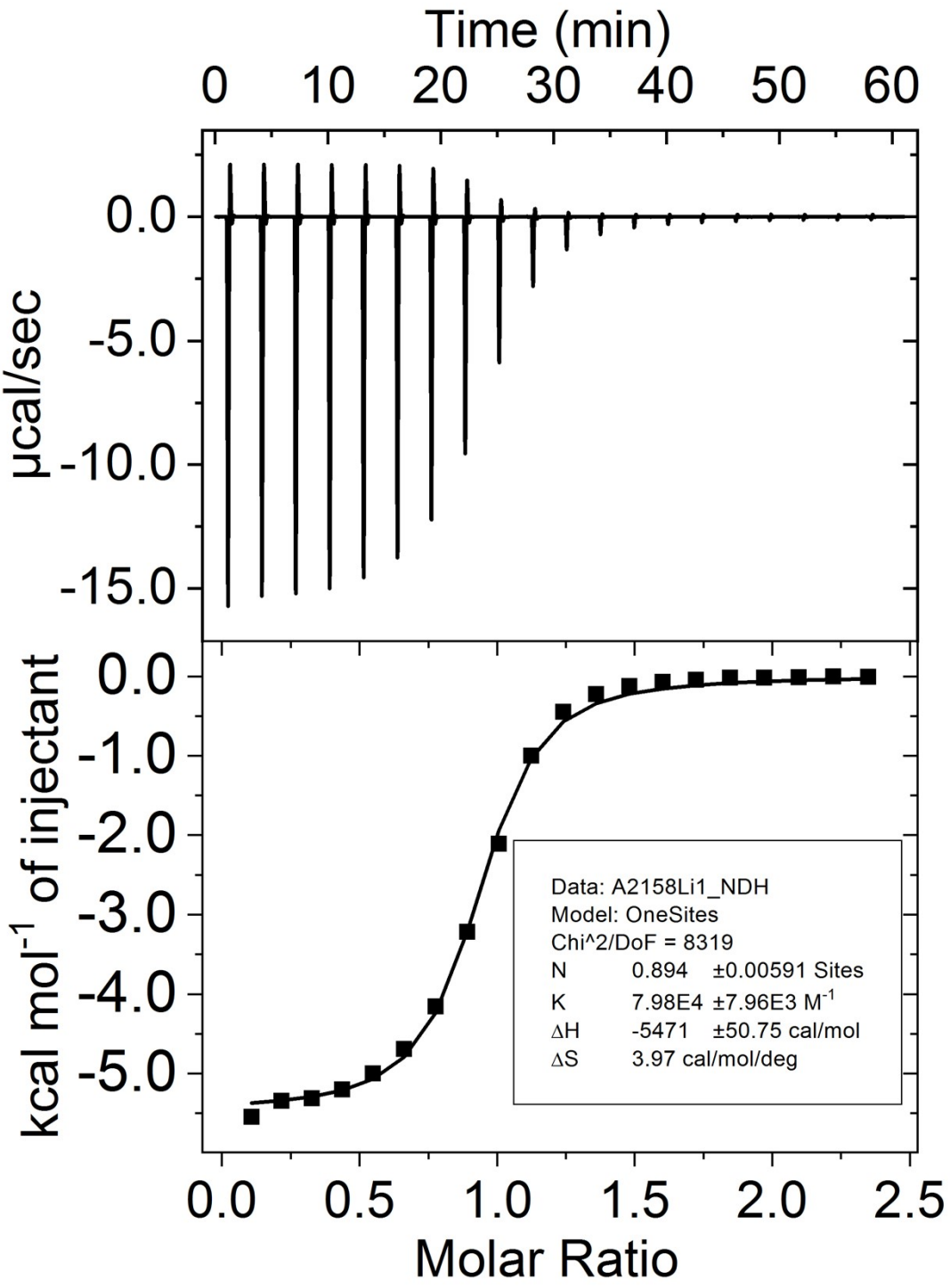

Figure S45. ITC profiles for the titration of I5 (0.9 m in the cell) with $LiBF_4$ (10.0 mM in syringe) in MeCN. The solid line represents the best non-linear fit of the data to a 1:1 binding model.

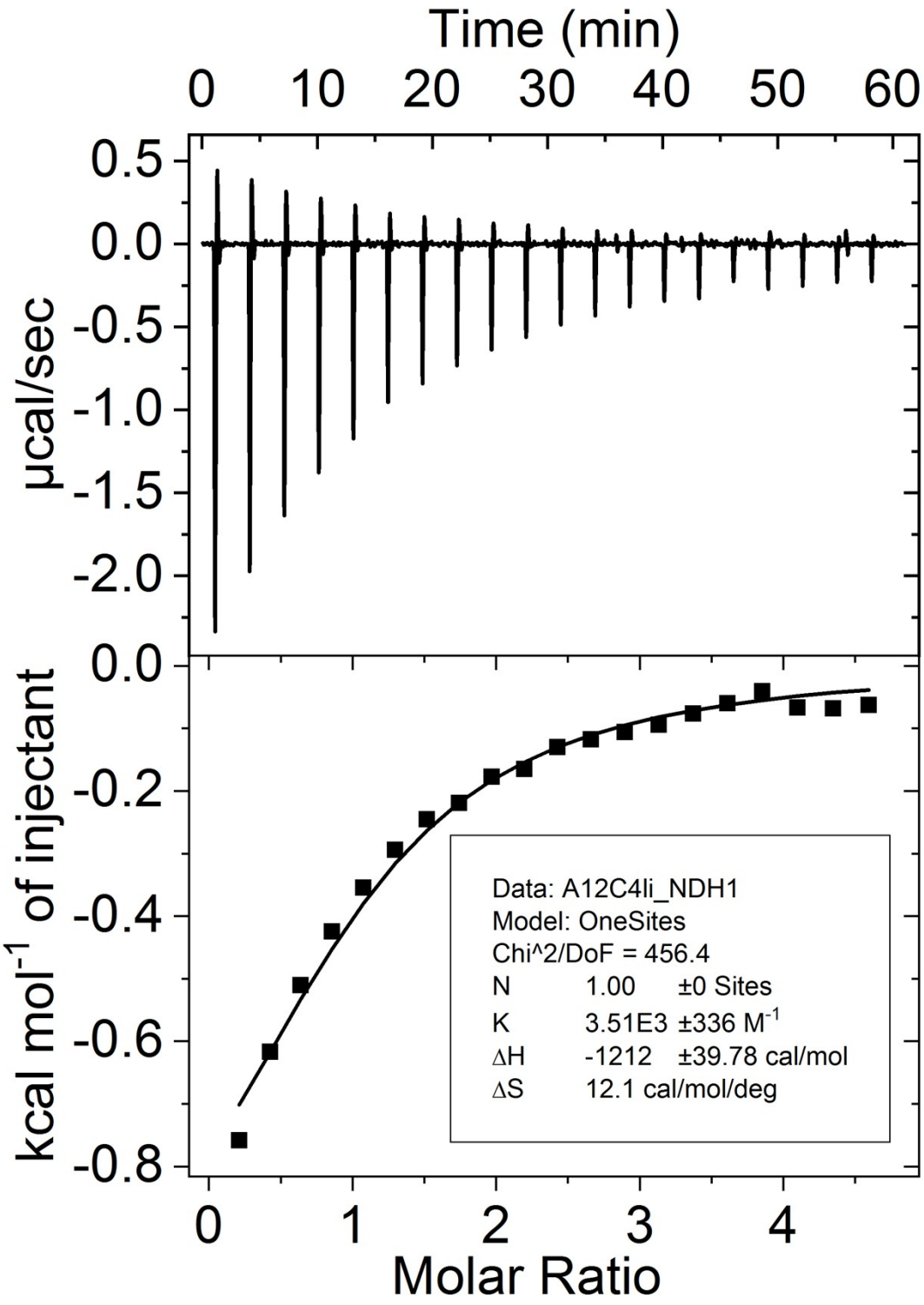

Figure S46. ITC profiles for the titration of $LiBF_4$ (0.4 mM in the cell) with 12-Crown-4 (10.0 mM in syringe) in MeCN. The solid line represents the best non-linear fit of the data to a 1:1 binding model.

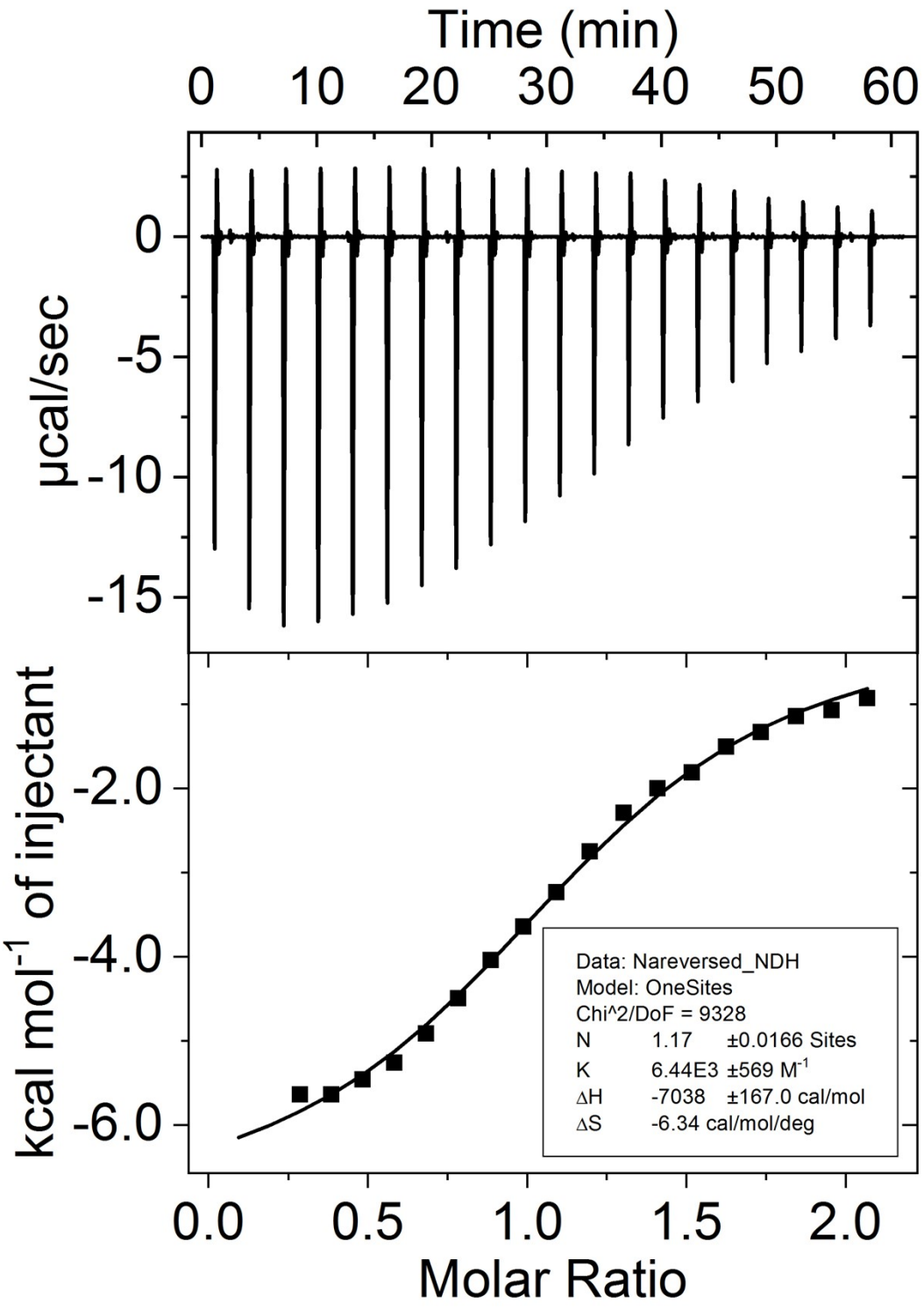

Figure S47. ITC profiles for the titration of $NaBF_4$ (1.0 mM the in the cell) with 12-Crown-4 (10.0 mM in syringe) in MeCN. The solid line represents the best non-linear fit of the data to a 1:1 binding model.

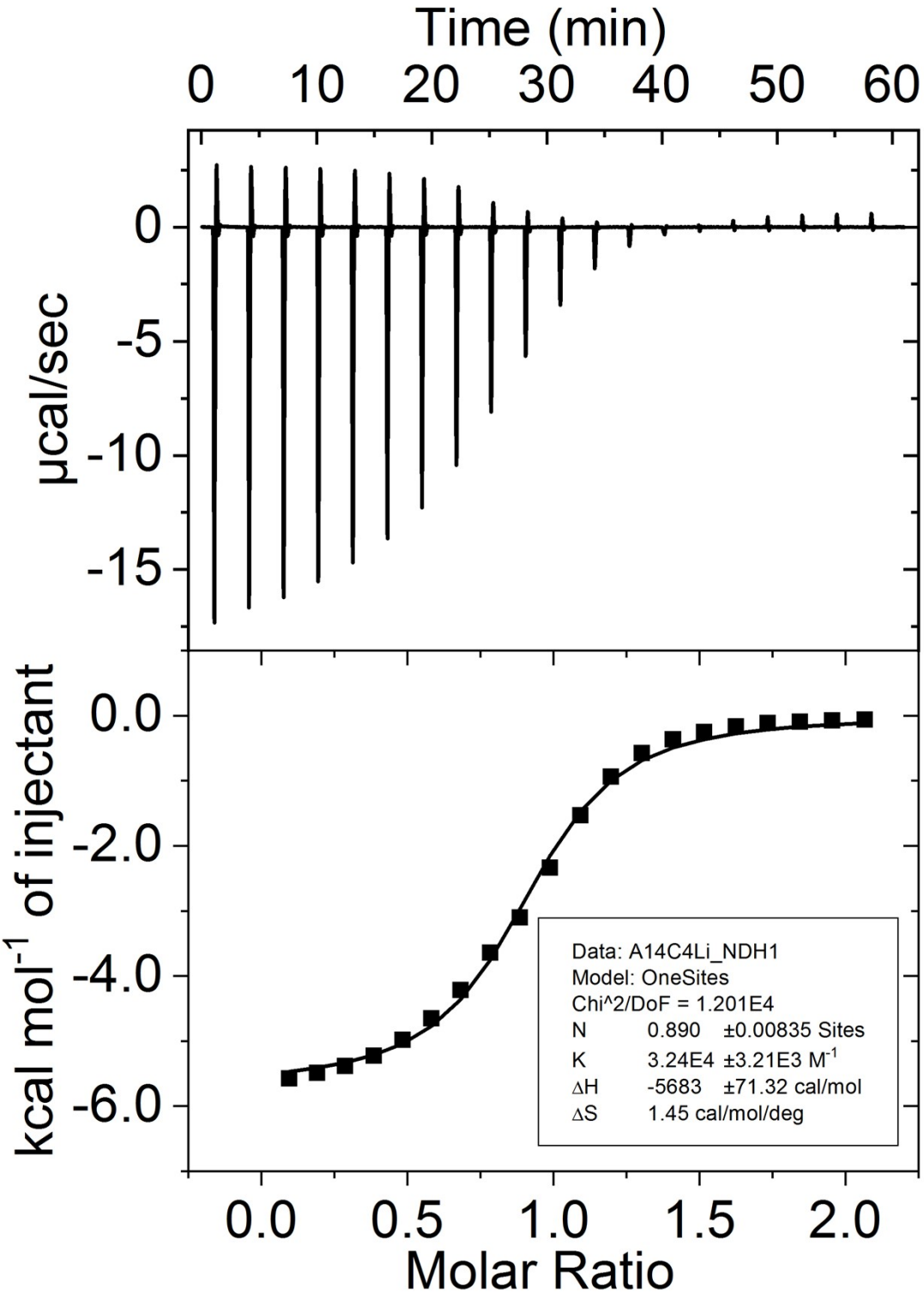

Figure S48. ITC profiles for the titration of DB-14-crown-4 (1.1 mM in the cell) with $LiBF_4$ (10.0 mM in syringe) in MeCN. The solid line represents the best non-linear fit of the data to a 1:1 binding model.

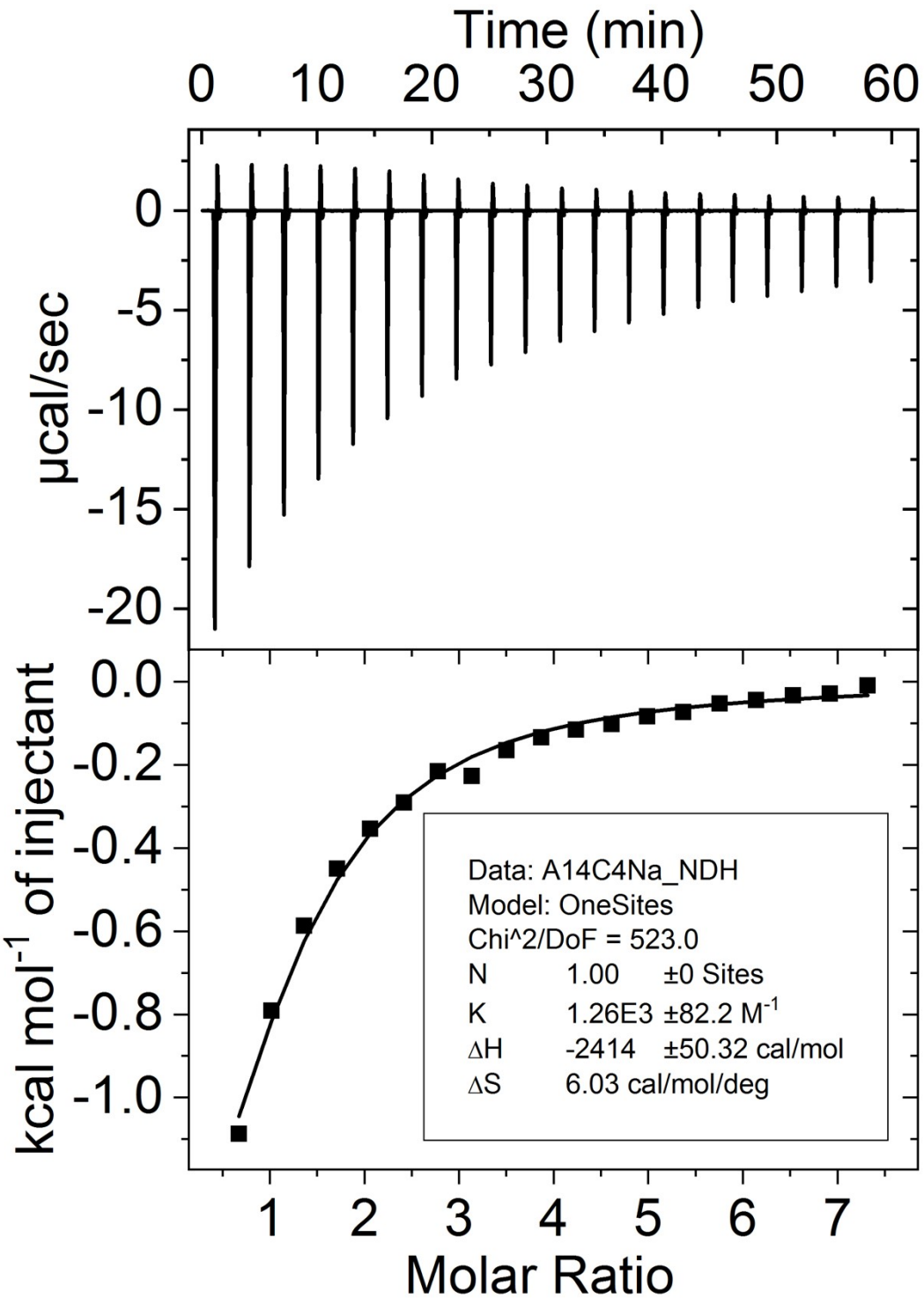

Figure S49. ITC profiles for the titration of DB-14-crown-4 (1.0 mM in the cell) with $NaBF_4$ (10.0 mM in syringe) in MeCN. The solid line represents the best non-linear fit of the data to a 1:1 binding model.

6. X-Ray Crystallography Data and Analysis

X-ray data and Analysis for I2

Single crystals of I2 were obtained as colorless blocks by slow evaporation of a sample dissolved in $CHCl_3$. X-ray diffraction data were measured on Bruker D8 Venture PHOTON II CMOS diffractometer equipped with a Cu Kα INCOATEC ImuS micro-focus source (λ = 1.54178 Å). Indexing was performed[S6] using APEX4 (Difference Vectors method). Data integration and reduction were performed[S7] using SaintPlus. Absorption correction was performed[S8] by the multi-scan method implemented in SADABS. The space group was determined using[S6] XPREP implemented in APEX3. The structure was solved using SHELXT[S9] and refined using SHELXL-2019/1[S10] (full-matrix least-squares on F2) through OLEX2 interface program[S11]. The ellipsoid plot was made with Platon [S12,S13]. Data and refinement conditions are shown in Table 1. CCDC deposition number: 2252048

Table S1 Crystal data and structure refinement for I2.	
Identification code	2046_1
Empirical formula	$C_{45}H_{66}N_2O_4$
Formula weight	698.99
Temperature/K	100.00
Crystal system	monoclinic
Space group	$P2_1/n$
a/Å	17.9216(2)
b/Å	10.15640(10)
c/Å	21.9165(3)
α/°	90
β/°	91.6817(6)
γ/°	90
Volume/Å^3	3987.50(8)
Z	4
ρ_{calc}g/cm^3	1.164
μ/mm^{-1}	0.567
F(000)	1528.0
Crystal size/mm^3	0.12 × 0.08 × 0.06
Radiation	CuKα (λ = 1.54178)
2Θ range for data collection/°	6.28 to 160.252
Index ranges	-22 ≤ h ≤ 21, -12 ≤ k ≤ 12, -27 ≤ l ≤ 27
Reflections collected	46152
Independent reflections	8366 [R_{int} = 0.0407, R_{sigma} = 0.0260]
Data/restraints/parameters	8366/0/460
Goodness-of-fit on F^2	1.028
Final R indexes [I>=2σ (I)]	R_1 = 0.0367, wR_2 = 0.0851
Final R indexes [all data]	R_1 = 0.0444, wR_2 = 0.0905
Largest diff. peak/hole / e Å^{-3}	0.26/-0.18

7. Computational Analysis

Structural Optimization and Binding Energy Analysis: The Cartesian coordinates for the calculations were directly created using GaussView 6 program. All optimizations were performed with density functional theory (DFT) in the Orca program[S14] (version 4.2.1) using the Becke '88 exchange and Lee-Yang-Parr correlation (BLYP) functional[S15], the Ahlrich's double zeta Def2-SVP or triple zeta valence Def2-TZVP basis sets[S16] with geometrical counterpoise (gCP) scheme[S17], and Grimme's third-generation dispersion correction[S18] with Beck Johnson damping (D3BJ). In order to speed up the DFT optimizations, the Coulomb integral[S19] and numerical chain-of-sphere integration[S20] for the HF exchanges (RIJCOSX) method was applied with the Def2/J auxiliary basis (AuxJ)[S21]. All optimizations were performed in an acetonitrile continuum with the Conductor-like Polarizable Continuum Model (CPCM) in Orca. In order to calculate binding energy, the structures of ionophores complexed with ions were first optimized, and the corresponding energies are represented as E(Li^+/Na^+⊂I#). Single point energies were subsequently calculated for the ionophore and ions and designated as E(I#) and E(Na^+/Li^+), respectively. The binding energy E was defined as E = (E(Li^+/Na^+⊂I#))- E(I#)- E(Na^+/Li^+).

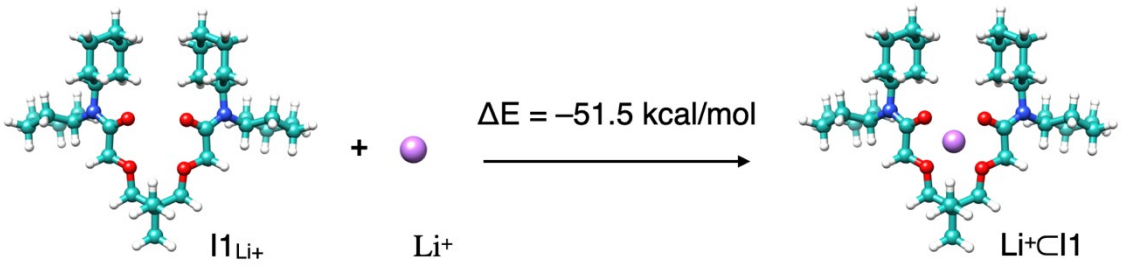

Figure S50. The binding energy of Li^+⊂I1

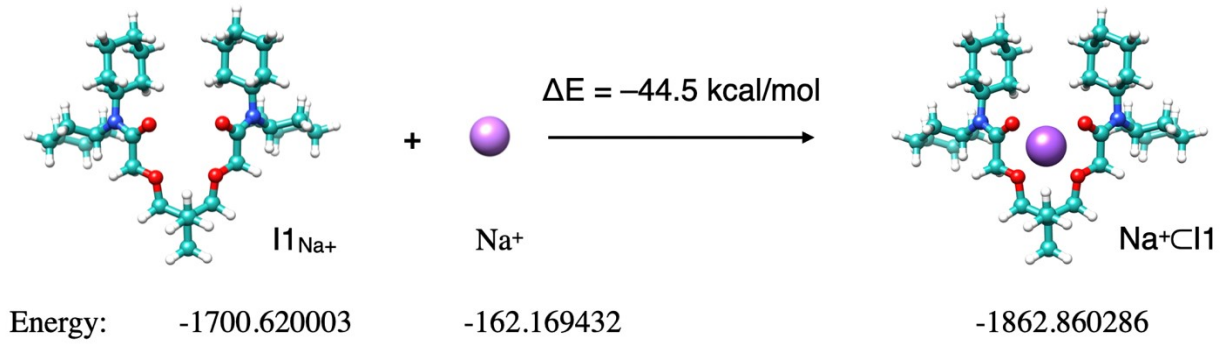

Energy: -1700.620003 -162.169432 -1862.860286

Figure S51. The binding energy of $Na^+ \subset I1$

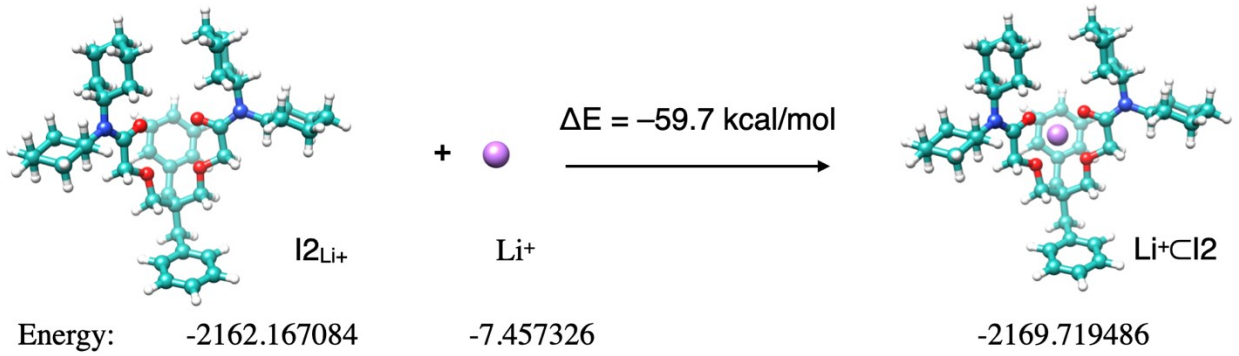

Energy: -2162.167084 -7.457326 -2169.719486

Figure S52. The binding energy of $Li^+ \subset I2$

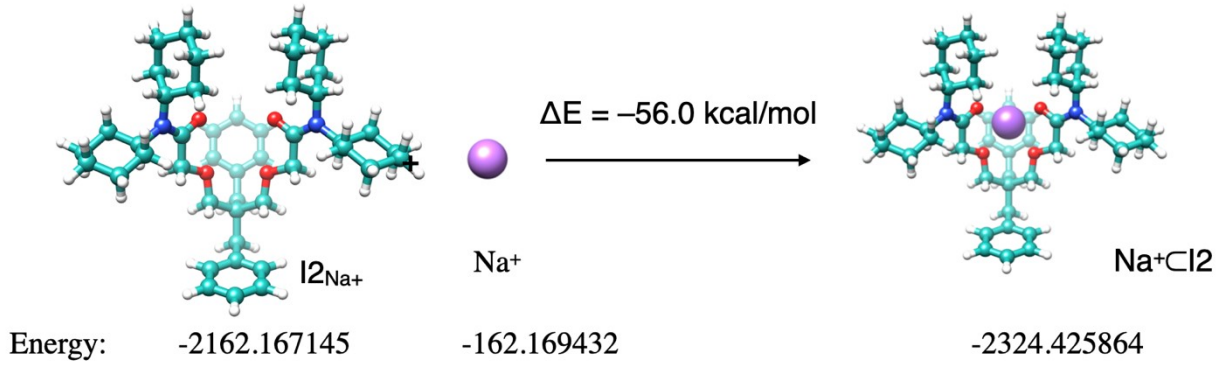

Energy: -2162.167145 -162.169432 -2324.425864

Figure S53. The binding energy of $Na^+ \subset I2$

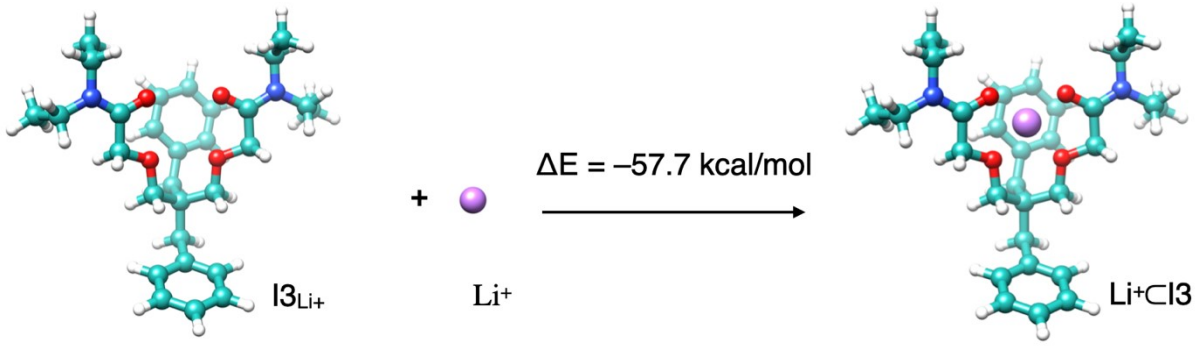

Energy:	-1538.851651	-7.457326	-1546.4008681

Figure S54. The binding energy of $Li^+ \subset I3$

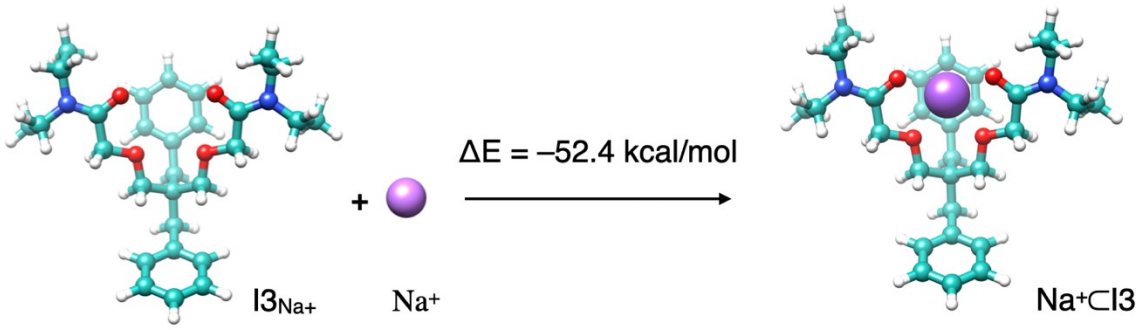

Energy:	-1538.856160	-162.169432	-1701.109174

Figure S55. The binding energy of $Na^+ \subset I3$

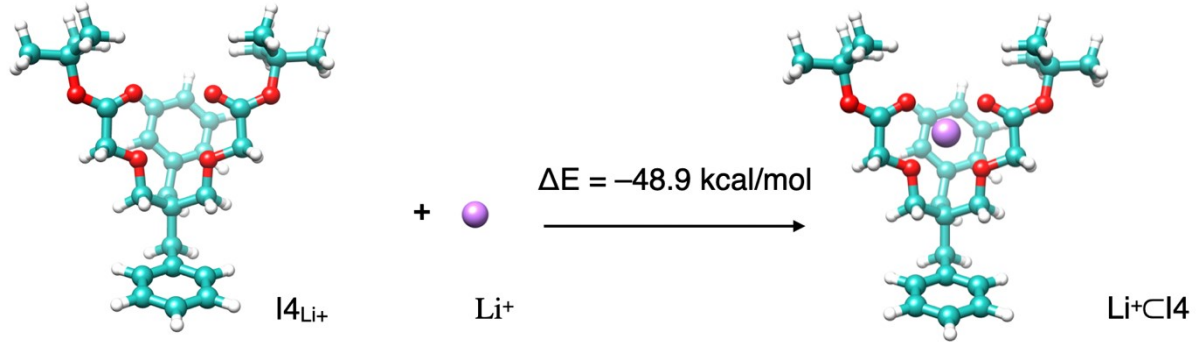

Energy:	-1578.585877	-7.457326	-1586.121152

Figure S56. The binding energy of $Li^+ \subset I4$

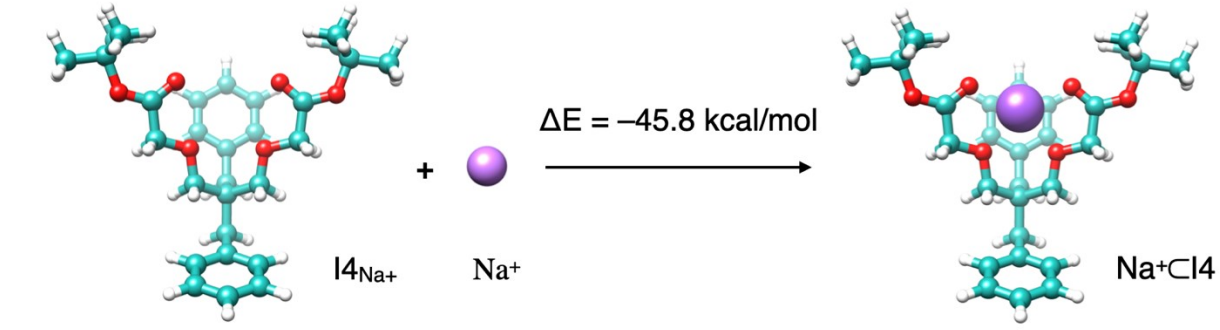

Figure S57. The binding energy of $Na^+ \subset I4$

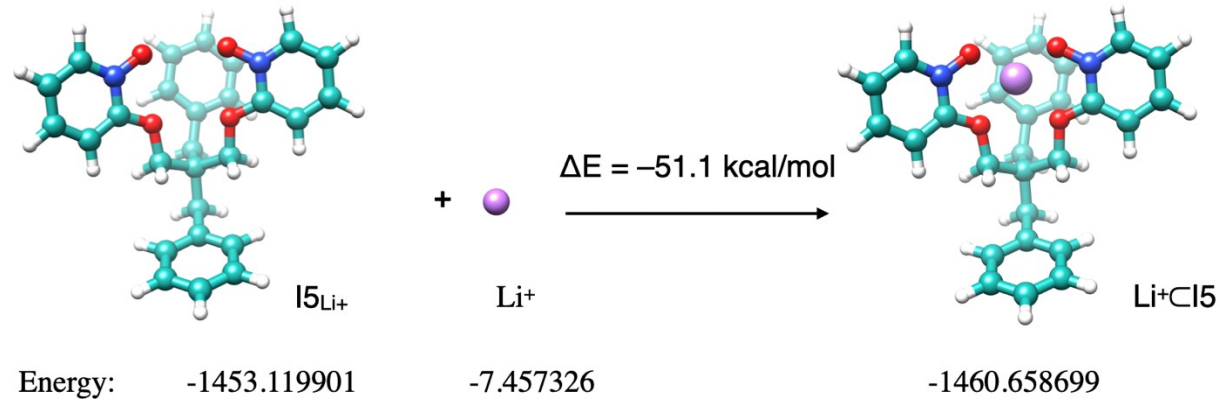

Figure S58. The binding energy of $Li^+ \subset I5$

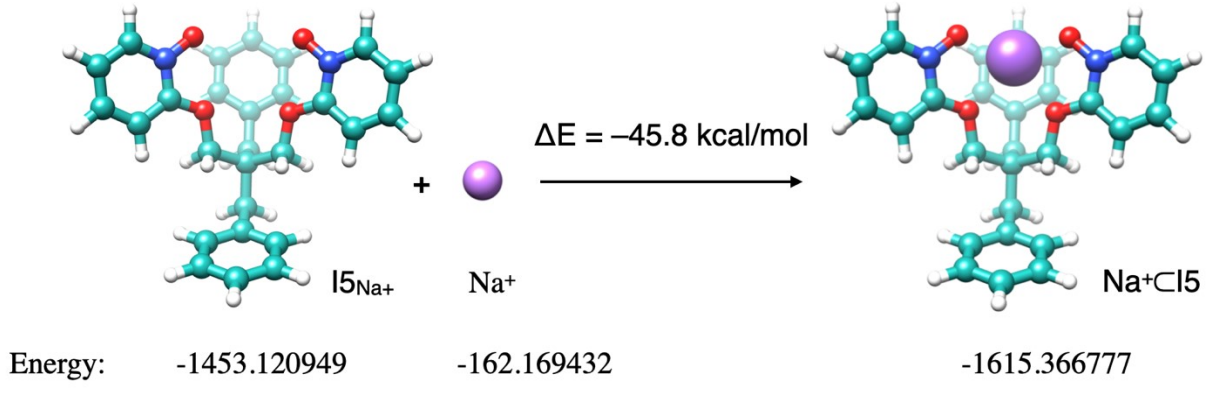

Figure S59. The binding energy of $Na^+ \subset I5$

Table S2. Binding energies in acetonitrile continuum at BLYP-SVP level

Entry	Electronic Energy (Hartree)	Binding Energy (kcal/mol)
Li^+	-7.457326	N.A.
Na^+	-162.169432	N.A.
$I1_{Li+}$	-1700.615359	N.A.
$I1_{Na+}$	-1700.620003	N.A.
$Li^+\subset I1$	-1708.154752	-51.5
$Na^+\subset I1$	-1862.860286	-44.5
$I2_{Li+}$	-2162.167084	N.A.
$I2_{Na+}$	-2162.167145	N.A.
$Li^+\subset I2$	-2169.719486	-59.7
$Na^+\subset I2$	-2324.425864	-56.0
$I3_{Li+}$	-1538.851651	N.A.
$I3_{Na+}$	-1538.856160	N.A.
$Li^+\subset I3$	-1546.4008681	-57.7
$Na^+\subset I3$	-1701.109174	-52.4
$I4_{Li+}$	-1578.585877	N.A.
$I4_{Na+}$	-1578.590162	N.A.
$Li^+\subset I4$	-1586.121152	-48.9
$Na^+\subset I4$	-1740.832583	-45.8
$I5_{Li+}$	-1453.119901	N.A.
$I5_{Na+}$	-1453.120949	N.A.
$Li^+\subset I5$	-1460.658699	-51.1
$Na^+\subset I5$	-1615.366777	-47.9

Electrostatic Potential Map (ESP) Molecular structures were first optimized using the ORCA program as described above. Then, the optimized structures and their wavefunction files were used for ESP calculation[S22] using Multiwfn 3.6 program through function 5.

Calculation of partial charges: Partial atomic charges were calculated based on atomic dipole corrected Hirshfeld population method[S23] using Multiwfn 3.6 program through function 7.

Visualization of Noncovalent Interactions: Independent Gradient Model based on Hirshfeld partition of molecular density (IGMH) analysis[S9,S10] is an approach to identify and visualize intermolecular interactions. Strong polar attractions and weak van der Waals contacts are visualized as an isosurface with blue and green colors, respectively. DFT-optimized structures were used as input files. The binding surface was calculated by Multiwfn 3.6 program[S26] through function 20 (visual study of weak interaction) and visualized by Chimera[S27].

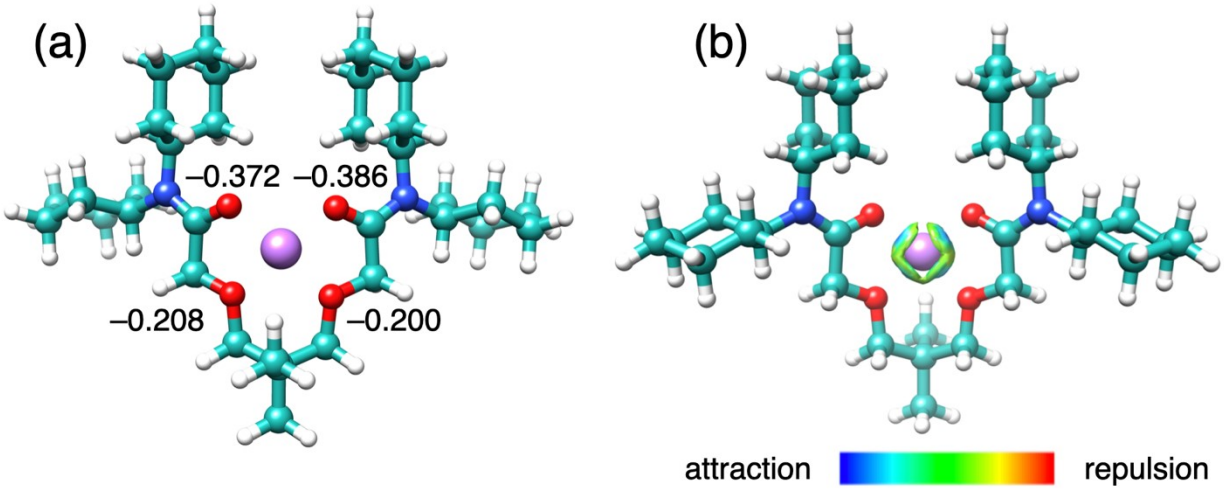

Figure S60. (a) Partial charges and (b) RGMH analysis of $Li^{+}\subset$I1 showing a noncovalent interaction isosurface of $\delta g^{inter} = 0.005$ a.u; color coding in the electron density range of –0.05<sign (λ_2)ρ <+0.05 a.u.

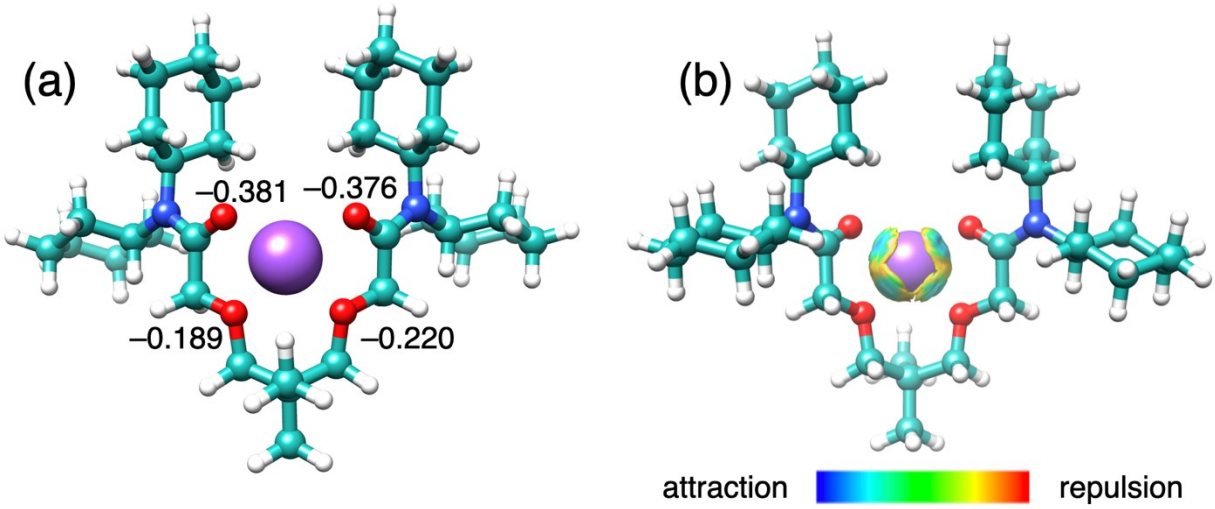

Figure S61. (a) Partial charges and (b) RGMH analysis of $Na^{+}\subset$I1 showing a noncovalent interaction isosurface of $\delta g^{inter} = 0.005$ a.u; color coding in the electron density range of –0.05<sign $(\lambda_2)\rho$ <+0.05 a.u.

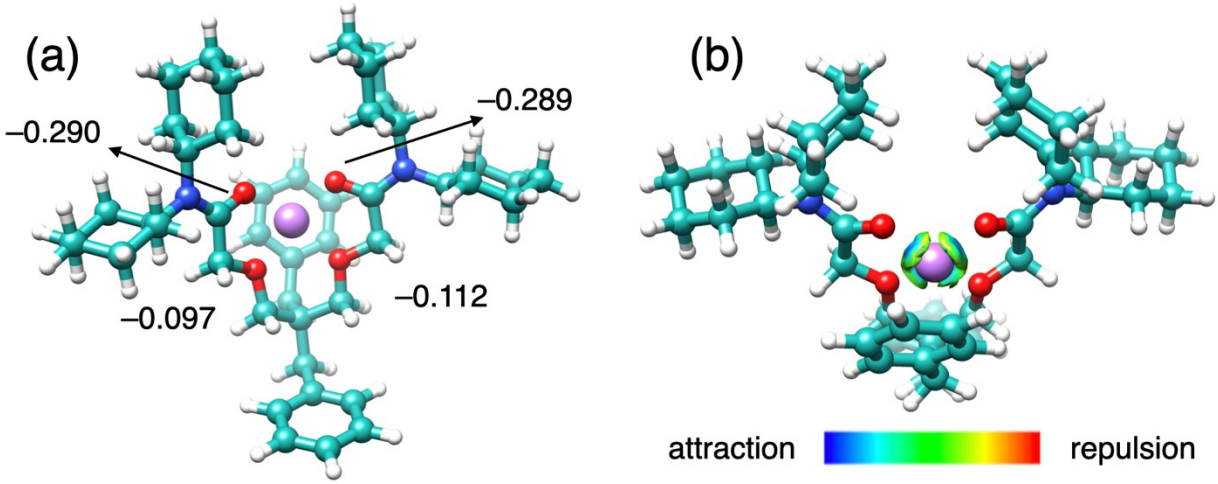

Figure S62. (a) Partial charges and (b) RGMH analysis of $Li^{+}\subset$I2 showing a noncovalent interaction isosurface of $\delta g^{inter} = 0.005$ a.u; color coding in the electron density range of –0.05<sign $(\lambda_2)\rho$ <+0.05 a.u.

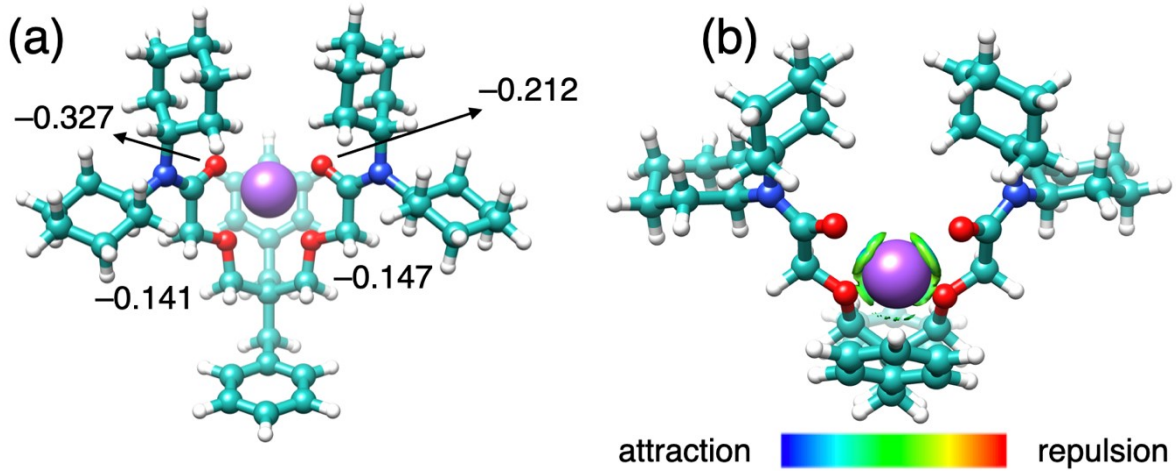

Figure S63. (a) Partial charges and (b) RGMH analysis of $Na^{+}\subset I2$ showing a noncovalent interaction isosurface of $\delta g^{inter} = 0.005$ a.u; color coding in the electron density range of –0.05<sign $(\lambda_2)\rho$ <+0.05 a.u.

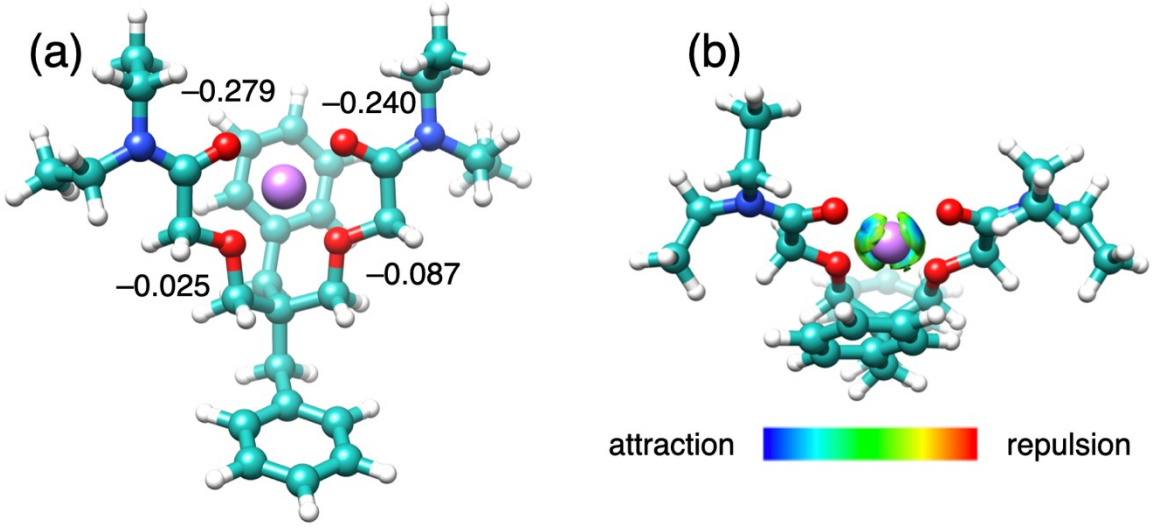

Figure S64. (a) Partial charges and (b) RGMH analysis of $Li^{+}\subset I3$ showing a noncovalent interaction isosurface of $\delta g^{inter} = 0.005$ a.u; color coding in the electron density range of –0.05<sign $(\lambda_2)\rho$ <+0.05 a.u.

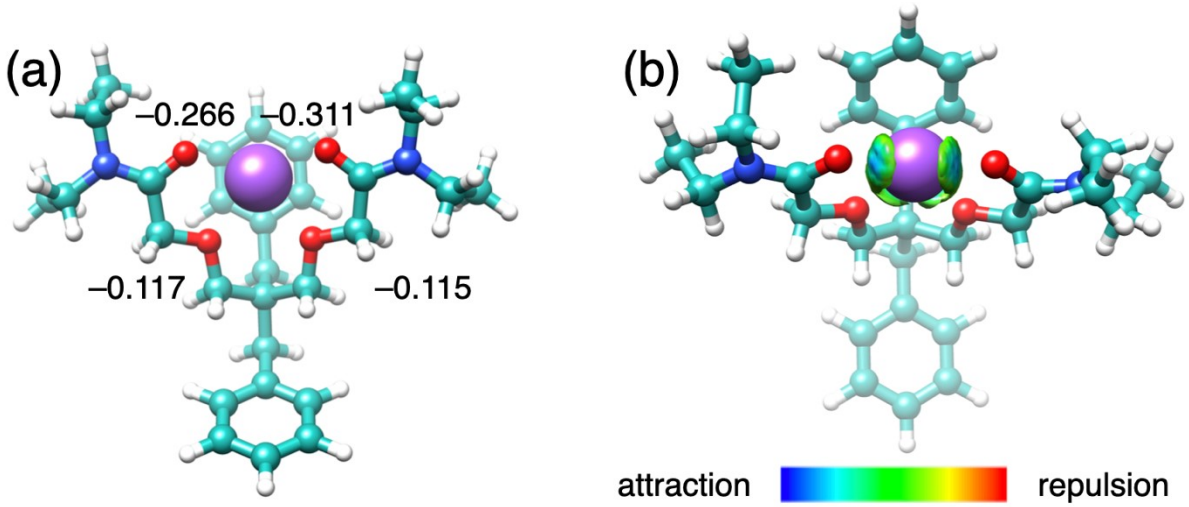

Figure S65. (a) Partial charges and (b) RGMH analysis of $Na^{+}\subset$I3 showing a noncovalent interaction isosurface of $\delta g^{inter} = 0.005$ a.u; color coding in the electron density range of –0.05<sign $(\lambda_2)\rho$ <+0.05 a.u.

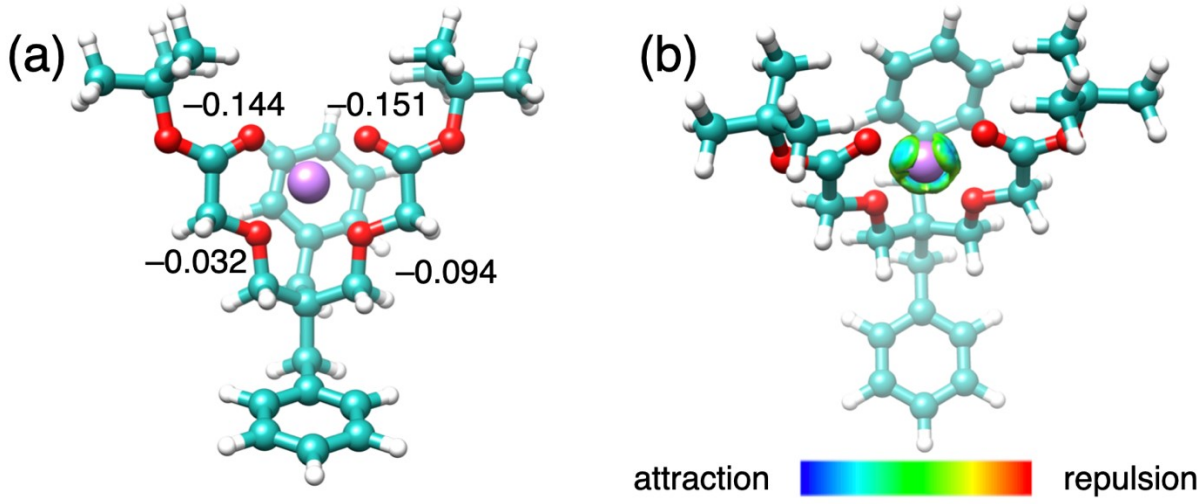

Figure S66. (a) Partial charges and (b) RGMH analysis of $Li^{+}\subset$I4 showing a noncovalent interaction isosurface of $\delta g^{inter} = 0.005$ a.u; color coding in the electron density range of –0.05<sign $(\lambda_2)\rho$ <+0.05 a.u.

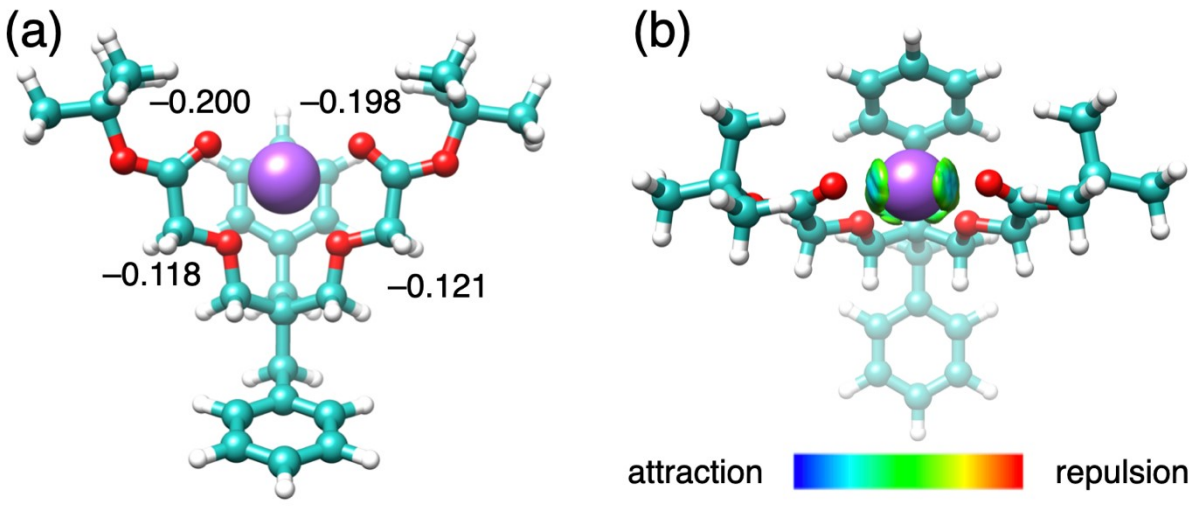

Figure S67. (a) Partial charges and (b) RGMH analysis of $Na^{+}\subset I4$ showing a noncovalent interaction isosurface of $\delta g^{inter} = 0.005$ a.u; color coding in the electron density range of –0.05<sign $(\lambda_2)\rho$ <+0.05 a.u.

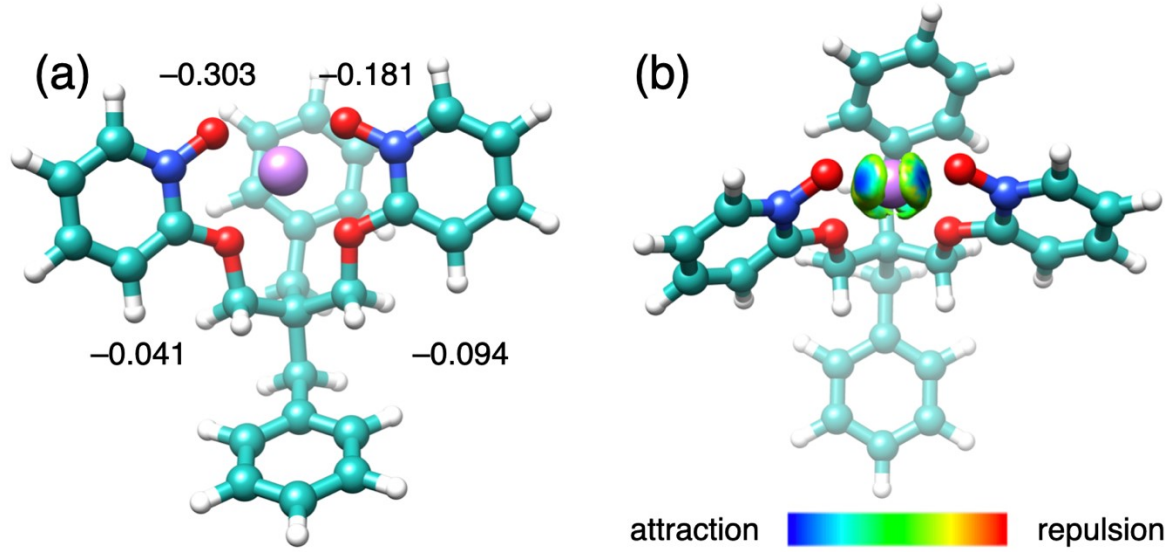

Figure S68. (a) Partial charges and (b) RGMH analysis of $Li^{+}\subset I5$ showing a noncovalent interaction isosurface of $\delta g^{inter} = 0.005$ a.u; color coding in the electron density range of –0.05<sign $(\lambda_2)\rho$ <+0.05 a.u.

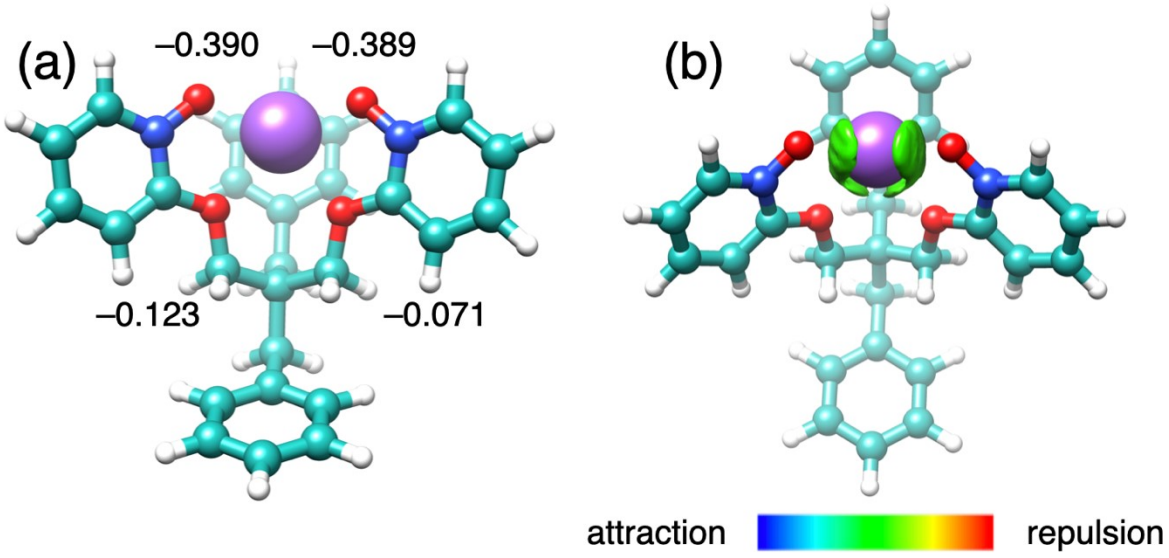

Figure S69. (a) Partial charges and (b) RGMH analysis of $Na^+ \subset$I5 showing a noncovalent interaction isosurface of $\delta g^{inter} = 0.005$ a.u; color coding in the electron density range of –0.05<sign $(\lambda_2)\rho$ <+0.05 a.u.

8. Solid-Liquid Extraction

A solution of receptor I5 (1 mM, 1 mL) in $CDCl_3$ was mounted on top of an excess amount of solid LiCl, NaCl, KCl or a mixture of the salts. The mixture was sonicated for 5 min. The resulting solution was pipetted into an NMR tube and measured by ^{1}H NMR spectroscopy. The stripping of Li^+ was realized by adding D_2O (1 mL) to the extractant, and the solution mixture was vortexed for 1 min, after which the organic phase was separated and measure by ^{1}H NMR spectroscopy.

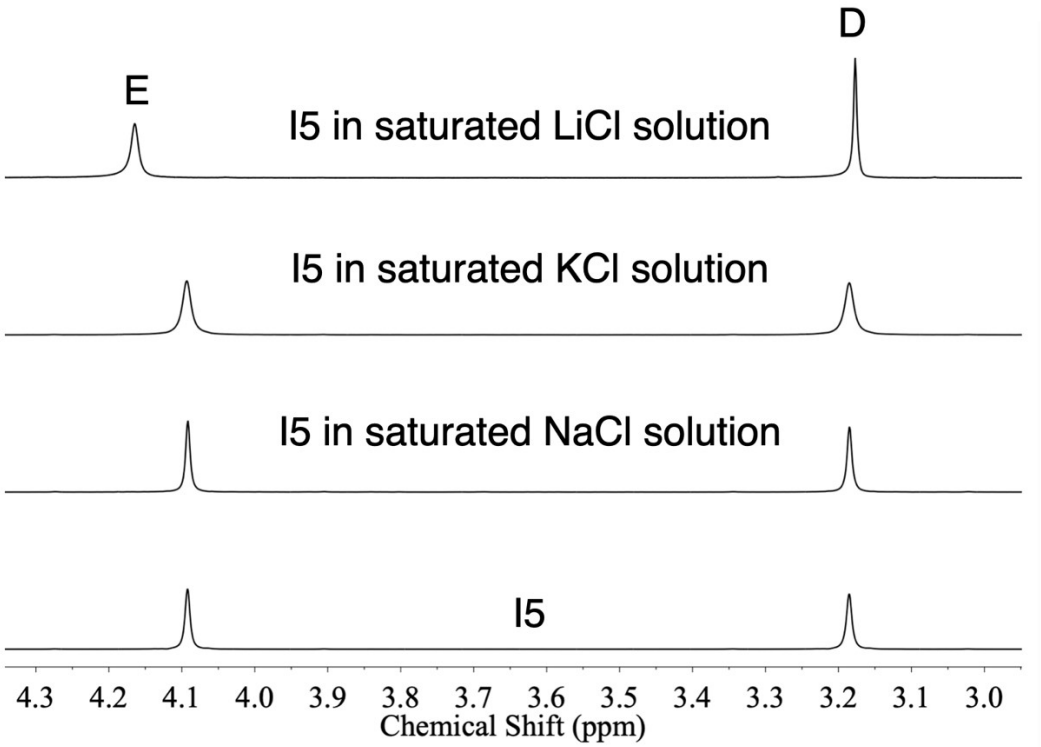

Figure S70. ^{1}H NMR (400 MHz, $CDCl_3$) spectra of I5 in the presence of saturated LiCl, NaCl and KCl solution in $CDCl_3$.

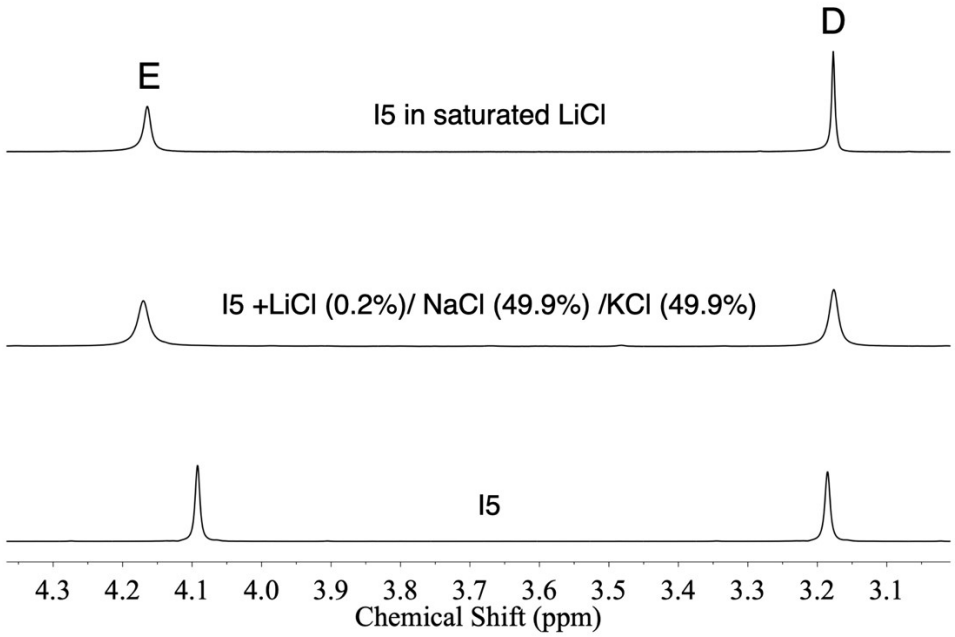

Figure S71. ^{1}H NMR (400 MHz, $CDCl_3$) spectra of I5 to track the solid-liquid extraction of 0.2% LiCl in the presence of a large excess amount of NaCl and KCl.

9. Reference

S1 S. K. Jana, M. Maiti, P. Dey and B. Maji, *Org. Lett.*, 2022, **24**, 1298–1302.

S2 Y. Huang, X. Li, L. Chen, G. Luo, D. Tao, J. Sun, Z. Qiu, Y. Chao and W. Zhu, *New J. Chem.*, 2022, 3134–3139.

S3 E. Metzger, R. Aeschimann, M. Egli, G. Suter, R. Dohner, D. Ammann, M. Dobler and W. Simon, *Helv. Chim. Acta*, 1986, **69**, 1821–1828.

S4 http://supramolecular.org.

S5 D. Brynn Hibbert and P. Thordarson, *Chem. Commun.*, 2016, **52**, 12792–12805.

S6 Bruker (2022). APEX4. Bruker AXS Inc., Madison, Wisconsin, USA.

S7 Bruker (2013). SAINT v8.34A. Bruker AXS Inc., Madison, Wisconsin, USA.

S8 L. Krause, R. Herbst-Irmer, G. M. Sheldrick and D. Stalke, *J. Appl. Crystallogr.*, 2015, **48**, 3–10.

S9 G. M. Sheldrick, *Acta Crystallogr. Sect. A*, 2015, **71**, 3–8.

S10 G. M. Sheldrick, *Acta Crystallogr. Sect. C*, 2015, **71**, 3–8.

S11 O. V Dolomanov, L. J. Bourhis, R. J. Gildea, J. A. K. Howard and H. Puschmann, *J. Appl. Crystallogr.*, 2009, **42**, 339–341.

S12 R. W. W. Hooft, L. H. Straver and A. L. Spek, *J. Appl. Crystallogr.*, 2008, **41**, 96–103.

S13 A. L. Spek, *Acta Crystallogr., Sect. D Biol. Crystallogr*, 2009, **65**, 148–155.

S14 F. Neese, *Rev. Comput. Mol. Sci*, 2012, **2**, 73–78.

S15 A. D. Becke, *J. Chem. Phys*, 1993, **98**, 5648–5652.

S16 F. Weigend and R. Ahlrichs, *Phys. Chem. Chem. Phys.*, 2005, **7**, 3297–3305.

S17 H. Kruse and S. Grimme, *J. Chem. Phys.*, 2012, **136**, 154101.

S18 S. Grimme, J. Antony, S. Ehrlich and H. Krieg, *J. Chem. Phys.*, 2010, **132**, 154104.

S19 F. Weigend, *Phys. Chem. Chem. Phys.*, 2006, **8**, 1057–1065.

S20 R. Izsák and F. Neese, *J. Chem. Phys.*, 2011, **135**, 144105.

S21 G. L. Stoychev, A. A. Auer and F. Neese, *J. Chem. Theory Comput.*, 2017, **13**, 554–562.

S22 J. Zhang and T. Lu, *Phys. Chem. Chem. Phys.*, 2021, **23**, 20323–20328.

S23 T. LU and F. CHEN, *J. Theor. Comput. Chem.*, 2012, **11**, 163–183.

S24 T. Lu and Q. Chen, *J. Comput. Chem.*, 2022, **43**, 539–555.

S25 C. Lefebvre, G. Rubez, H. Khartabil, J. C. Boisson, J. Contreras-García and E. Hénon, *Phys. Chem. Chem. Phys.*, 2017, **19**, 17928–17936.

S26 T. Lu and F. Chen, *J. Comput. Chem.*, 2012, **33**, 580–592.

S27 E. F. Pettersen, T. D. Goddard, C. C. Huang, G. S. Couch, D. M. Greenblatt, E. C. Meng and T. E. Ferrin, *J. Comput. Chem.*, 2004, **25**, 1605–1612.